remote sensing

MDPI

Article

Exploring Sentinel-1 Radar Polarisation and Landsat Series Data to Detect Forest Disturbance from Dust Events: A Case Study of the Paphos Forest in Cyprus

Christos Theocharidis [1,2,*], Marinos Eliades [1], Polychronis Kolokoussis [3], Milto Miltiadou [4], Chris Danezis [1,2], Ioannis Gitas [5], Charalampos Kontoes [6] and Diofantos Hadjimitsis [1,2]

[1] ERATOSTHENES Center of Excellence, Limassol 3036, Cyprus; marinos.eliades@eratosthenes.org.cy (M.E.); chris.danezis@cut.ac.cy (C.D.); d.hadjimitsis@cut.ac.cy (D.H.)
[2] Department of Civil Engineering and Geomatics, Faculty of Engineering and Technology, Cyprus University of Technology, Limassol 3036, Cyprus
[3] School of Rural and Surveying Engineering, National Technical University of Athens, 15780 Athens, Greece; pol@survey.ntua.gr
[4] Department of Computer Science, University of Exeter, Exeter EX4 4PY, UK; m.miltiadou@exeter.ac.uk
[5] School of Forestry and Natural Environment, Aristotle University of Thessaloniki, 541 24 Thessaloniki, Greece
[6] BEYOND Center, IAASARS, National Observatory of Athens, 152 36 Penteli, Greece; kontoes@noa.gr
* Correspondence: christos.theocharidis@eratosthenes.org.cy

Abstract: Monitoring forest health has become essential due to increasing pressures caused by climate change and dust events, particularly in semi-arid regions. This study investigates the impact of dust events on forest vegetation in Paphos forest in Cyprus, which is a semi-arid area prone to frequent dust storms. Using multispectral and radar satellite data from Sentinel-1 and Landsat series, vegetation responses to eight documented dust events between 2015 and 2019 were analysed, employing BFAST (Breaks For Additive Season and Trend) algorithms to detect abrupt changes in vegetation indices and radar backscatter. The outcomes showed that radar data were particularly effective in identifying only the most significant dust events (PM10 > 100 $\mu g/m^3$, PM2.5 > 30 $\mu g/m^3$), indicating that SAR (Synthetic Aperture Radar) is more responsive to pronounced dust deposition, where backscatter changes reflect more substantial vegetation stress. Conversely, optical data were sensitive to a wider range of events, capturing responses even at lower dust concentrations (PM10 > 50 $\mu g/m^3$, PM2.5 > 20 $\mu g/m^3$) and detecting minor vegetation stress through indices like SAVI, EVI, and AVI. The analysis highlighted that successful detection relies on multiple factors beyond sensor type, such as rainfall timing and imagery availability close to the dust events. This study highlights the importance of an integrated remote sensing approach for effective forest health monitoring in regions prone to dust events.

Keywords: time-series analysis; SAR; BFAST; dust storm; forest degradation; forest phenology; decomposition; climate change

Academic Editor: Justin F Moat

Received: 10 February 2025
Revised: 23 February 2025
Accepted: 27 February 2025
Published: 28 February 2025

Citation: Theocharidis, C.; Eliades, M.; Kolokoussis, P.; Miltiadou, M.; Danezis, C.; Gitas, I.; Kontoes, C.; Hadjimitsis, D. Exploring Sentinel-1 Radar Polarisation and Landsat Series Data to Detect Forest Disturbance from Dust Events: A Case Study of the Paphos Forest in Cyprus. *Remote Sens.* **2025**, *17*, 876. https://doi.org/10.3390/rs17050876

1. Introduction

Dust storms, exacerbated by climate change, drought, and unsustainable management practices, are closely linked to forest degradation. These extreme phenomena further impact climate change by affecting the Earth's radiative balance and precipitation patterns [1–3]. Therefore, this forest decline disturbs the ecosystems' natural benefits and contributes significantly to the frequency and severity of dust storms. This emphasises the need for enhancing monitoring activities to provide the tools for sustainable forest management

practices and efforts to combat desertification and forest degradation [4]. Forests and trees make indispensable contributions to humanity and the planet Earth by creating jobs [5], conserving biodiversity, supporting livelihoods, and assisting in stabilising climate change by regulating the Earth's temperature and water flows [6]. Nowadays, forests cover 31% of the land surface, and their habitat area is decreasing, where more than 20 million km^2 of the world's forests have been degraded [3]. Forests play a crucial role in carbon sequestration and climate change mitigation [7–9]. Forest degradation negatively impacts the smooth functioning of ecosystem services and can lead to the creation of drylands, which are often the primary sources of sand and dust storms. This degradation, often caused by various socio-economic circumstances, gradually reduces the forest's capacity to provide goods and services [10,11]. The effects of this procedure become visible only after a long period [12], indicating the gradual degradation of forests [13–15]. Of course, degradation in forests can result from other factors, such as commercial agriculture [16], illegal logging [17], wildfires [18], pollution [19], invasive species [20], or pest infestation [21].

The main objective of the European Union (EU) forest strategy for 2030 is the adaptation of Europe's forests to the new climate conditions and extreme weather phenomena due to ongoing climate change. Widening the EU's forests through afforestation is one of the fundamental goals of this strategy [22]. However, the drought conditions in semi-arid regions are projected to intensify in the near future, undermining the success of afforestation, which depends on trees' capacity to adapt to drought [23]. As our understanding of climate change deepens, we realise that a combination of various environmental, meteorological, and anthropogenic factors, as well as rainfall [24–26], photoperiod [27–29], and dust storms, may interact and simultaneously influence vegetation dynamics, the flowering period [30], and plant phenology [31].

During the last decades, studies indicated that the vegetation's flowering season has been extended due to climate change [32–34], influencing people's perception of the effects of the climate crisis on forests [35]. Monitoring plant phenology is crucial for preserving resilience within an ecosystem at both regional and global levels since the vegetation's life cycle has a high sensitivity to climate change; the so-called phenophases are vital biological indicators to understand how these ecosystems have been affected by climate change and how they will face the upcoming environmental changes in the following years [36–38].

Numerous techniques have been developed to monitor vegetation dynamics effectively, including in-situ observations [39,40], digital repeat photography [41–43], remote sensing [44–47], and integrations between the prior methods [48–50]. From the monitoring techniques mentioned above, remote sensing has the significant advantage of delivering large-scale multi-temporal images in contrast with the other methods [51,52]. A variety of sensors have played their part in vegetation dynamics, including multispectral [53–55], radar [56–59], Lidar [60,61], Unmanned Aerial Vehicle (UAV) [62–64], and mixtures between the sensors [65–68]. Nevertheless, limitations in optical remote sensing sensors, like lack of data due to cloud coverage, may be resolved using Synthetic Aperture Radar (SAR) satellite data (e.g., Sentinel-1) since this type of satellites can operate in any weather condition, even if thick clouds cover the area and the area has frequent rain activity [69]. Moreover, SAR can penetrate the forest canopy and retrieve information from above and below the tree crown, providing valuable data, giving the ability to understand phenological changes in various types of forests [70,71] and deriving accurate canopy heights metrics [72].

Delving further into the vegetation monitoring applications, various studies have been conducted during the years focusing on the effects of dust on vegetation [73–75]; some studies focused on the impact of cement dust in plants [76,77], while others assessed the effect of the desert dust [78–80]. Dust events can negatively affect forest health, leading to

destructive results combined with the absence of rainfall. High dust concentrations alter the rates of stomatal conductance and transpiration [81]. The layer of dust on the plant tissue blocks the stomata. It interrupts the gas exchange process while increasing the absorption of near-infrared solar spectral irradiance, resulting in elevated leaf temperature [82,83]. This can result in a reduction of transpiration during the mid-day and in an increase of the water loss at night [84]. The constant exposure of the plant to dust could lead to drought and water-stress conditions leading to xylem embolism [85]. The existence of air-filled tracheids and/or vessels in the plant anatomy can cause embolism resulting in a decreased efficiency of xylem transport. Moreover, it can have a negative impact by decreasing hydraulic conductance and limiting water supply to the transpiring leaves, posing a severe threat to the tree's health and survival [86]. Therefore, the dust can result in gradual or abrupt changes in the normal functioning of a forest, highlighting the need to monitor these changes.

Time-series analysis can assist in tracking forest decline by identifying abrupt shifts in vegetation dynamics trends. The trend parameter can be obtained through decomposition, which is a commonly used method to break down time series into components of seasonality, trend, and random noise, allowing for the identification of seasonal patterns and the removal of disturbances [87]. Various decomposition methods are available, each with their strengths and weaknesses. The classical decomposition by moving averages method is a traditional approach using moving averages to deal with additive or multiplicative seasonal components, but it may not capture changes over time [88]. Another method is the X-13 decomposition method, an advanced version of X-12 and X-11 for seasonal adjustment and descriptive analysis of time-series data. While it is a standard worldwide method that removes seasonal patterns, such as meteorological fluctuations from a time series, it does not handle outliers well [89]. The Loess decomposition method, developed by Cleveland [90], is a filtering methodology that uses locally fitted regression models to decompose a time series into noise, seasonality, and trend. It can quickly handle long-time and large amounts of trend and seasonal smoothing, but it may not be as efficient or flexible as other methods [90,91].

In contrast to the abovementioned methods, the BFAST (Breaks For Additive Season and Trend) algorithm, in addition to being a decomposition algorithm, can also be used as a change detection algorithm. BFAST is widely utilised for detecting trend and seasonal breaks in a time series [92], characterises both the direction and magnitude of the change, and has been applied in various applications like forest disturbance monitoring [93–95], wildfires [96–98], and land cover monitoring [99–101]. Furthermore, BFAST is an unsupervised algorithm that can automatically detect changes in data without needing prior training and can handle missing values, which is useful when dealing with passive remote sensing. However, the original BFAST algorithm is relatively slow; it has limited parameters and it tends to overestimate changes [102]. Building upon the original BFAST algorithm, BFAST Lite offers significant improvements in speed and flexibility while maintaining similar accuracy to the original BFAST, making it an improved choice over other decomposition and change detection methods due to its unique features and performance [102]. Additionally, there is the BFAST01 algorithm, which is the latest version of BFAST and checks for one major break in the time series, having also the ability to classify the type of change when it is identified. In addition the BFAST01 algorithm does not take into account seasonality but focuses on the trend and noise component, making it appropriate for data where seasonal variations are not a significant factor [103,104].

To the best of our knowledge, no studies have been conducted to identify forest disturbances due to dust events with radar polarisation. This paper aims to fill this gap by evaluating the ability of Sentinel-1 satellite data to identify forest disturbance caused by

eight dust events between 2014 and 2021 in the Paphos forest in Cyprus. Furthermore, ten Vegetation Indices (VIs) were utilised to detect possible forest disturbance from the three major dust events to compare the outcomes with the Sentinel-1 data.

2. Materials and Methods

2.1. Study Region

The Area of Interest (AoI) focuses on the north-western (NW) part of Cyprus in the "Paphos forest" located in the Paphos district in Cyprus. More specifically, the total study area is 196.36 km^2, focusing on the north-east (NE), east, and south-east (SE) AoIs regions, which are aligned with the non-shaded areas observed by the Sentinel-1 C-band sensor, following a descending orbit as described further in Section 2.3.1. Located in the northeastern end (33° east of Greenwich and 35° north of the Equator), Cyprus is the third-largest island in the Mediterranean Sea (Figure 1). Cyprus has an assortment of micro-climates and various terrains that are adequately sheltered as they can maintain a high diversity of species guiding into the shape of endemic biota [105,106]. Ancient authors, like Eratosthenes (275–195 B.C), reported that Cyprus had large areas of rich forests [107,108]. According to maps dating back to 1900, created by A. K. Bovilli [109] regarding the forest allocation in Cyprus, the chosen area of interest was forest, suggesting that it is one of the oldest remaining forests in Cyprus. *Pinus brutia Ten* is the dominant tree species in the Paphos forest, with additional old plantations of that species existing for 30 years; thus, the study area is distributed mainly up to 1400 m above sea level [105,108]. In addition, other predominant species exist in this mixed Mediterranean forest, such as smaller trees and bushes (*Quercus alnifolia*, *Genista fasselata*, *Sarcopoterium spinosum*), Thermo-Mediterranean riparian galleries (*Nerium oleander*, *Tamarix* spp.), sclerophyll shrubs (*Ceratonia siliqua*, *Rhamnus alaternus*, *Rhamnus oleides* subsp. *graeca*), and the Cypriot cedar (*Cedrus brevifolia*) where it is growing in the Cedar Valley on the slopes of Mount Tripylos [110].

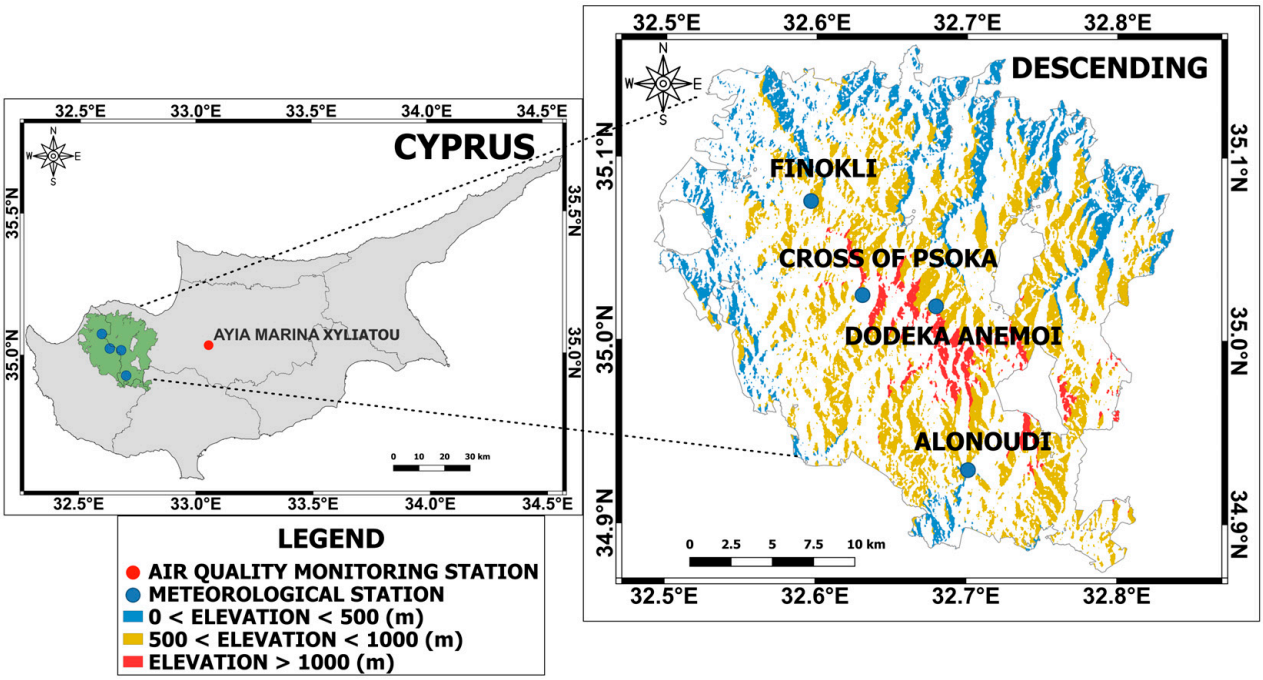

Figure 1. (**Left**): Paphos forest, Cyprus with green colour (AoI). (**Right**): Heights distribution of the AoI. The red dot indicates the location of the Ayia Marina Xyliatou air quality monitoring station. The blue dots concern the sites of the four meteorological stations of the Department of Meteorology, Cyprus.

2.2. Datasets

2.2.1. Satellite Data

This study utilised multispectral and radar satellite data from Landsat 7,8,9 and Sentinel-1 satellite images, respectively (Table 1). The data were obtained from the United States Geological Survey (USGS) data services (https://www.usgs.gov, accessed on 30 January 2025) via Google Earth Engine (GEE) and the Alaska Satellite Facility (ASF) (https://search.asf.alaska.edu/#/, accessed on 30 January 2025) and were processed in the georeferenced WGS 84/UTM zone 36N coordinate system. Combining data from the Landsat 7–8–9 satellites, the temporal resolution was significantly improved by 8 days of revisit time over the AoI, allowing for more frequent observations and a more detailed analysis of changes over time.

Table 1. The data summary utilised in the AoI shows the time frame, the number of processed images, and the total number of images used after filtering due to cloud coverage (Landsat-8) and high precipitation (Sentinel-1).

Satellite Mission	Spatial Resolution (m)	Time Frame	No. of Images	No. Images After Filtering
Landsat 7–8–9	30	October 2014–December 2021	354	242
Sentinel-1A/B	10	October 2014–November 2021	337	276

Moreover, the Moderate Resolution Imaging Spectroradiometer (MODIS) was used to assess the dust storm activity from satellite images for validation. Specifically, the dust score is derived by comparing radiances in specific AIRS spectral channels sensitive and insensitive to dust, with higher scores indicating a higher probability of dust presence. The data were sourced from https://worldview.earthdata.nasa.gov, (accessed on 30 January 2025) with 13.5 km/pixel resolution at nadir and twice daily temporal coverage [111]. The AIRS dust score was generally utilised to validate the timing and intensity of detected dust events, supplementing in-situ air quality data.

2.2.2. Meteorological Data

Studies have claimed that the high presence of soil moisture affects radar signal performance [112]. The study area can be described as a sparse forest; thus, the radar signal can easily reach the ground, penetrating the forest canopy and affecting the radar measurements when the soil moisture is high. Since SAR signal performance can be influenced by soil moisture, precipitation events were considered to assess their potential impact on SAR backscatter measurements. According to the Department of Meteorology, any precipitation exceeding 0.2 mm is classified as a rainy day. To minimise potential distortions caused by soil moisture, this study used precipitation data from four meteorological stations. More specifically, from the Alonoudi, Cross of Psoka, Dodeka Anemoi, and Finokli stations, precipitation data were collected for 2014–2019. For the years 2020 and 2021, data were derived from the Cross of Psoka station since the other three meteorological stations in the forest (Finokli, Dodeka Anemoi, Alonoudi) showed many gaps in their data, making them unable to provide satisfactory results. The data were obtained from the Department of Meteorology through a request process since they do not have an open access policy.

2.2.3. Air Quality Data

For validation purposes, air quality data were sourced from the Ayia Marina Xyliatou station, which was chosen for its strategic location approximately 20 km east of the Paphos forest (35.04N; 33.06E) and at an elevation of 535 m above sea level (Figure 1). This station was chosen since it measures continuously and updates the data in real-time of the

Particulate Matter in the air, with a diameter of 10 (PM10) and 2.5 (PM2.5) micrometres or less, which were needed for this study.

2.3. Methodology

2.3.1. Satellite Images Processing

The Department of Forest in Cyprus provided the AoI's boundaries. To "avoid" noise within our data, any area burnt between 1992 and 2021 was extracted since satellites can easily detect forest stands when they are under regeneration status [113]. The Department of Forests provided shapefile data containing polygons with the burnt areas. More specifically, a fire broke out at the north-west part of the AoI on 06 March 2003, which was mapped and removed by implementing the Normalised Difference Vegetation Index (NDVI) [114] and the Normalised Burned Ratio (NBR) [115] downloaded from a Landsat–5 image. In addition, an aspect map was generated from the ASTER Global Digital Elevation Model (GDEM), and the aspect directions NE, E, and SE (22.5–157.5 degrees) were included in the study area as earlier mentioned, which created the final AoI with the non-shaded areas (Figure 1).

For pre-processing purposes of the Sentinel-1 GRD images, all the standard processing methods were exploited in SNAP software (v.10.0.0) to derive the backscatter coefficient (*Thermal noise removal*, *Apply Orbit File*, *Calibration*, *Speckle Filter*, *Terrain Correction*). The median filter was used for speckle filtering since the forest is a dynamic place with many high shifts concerning the SAR signal scattering (e.g., movement of leaves). Therefore, it is considered an effective filter to remove possible outliers. After that, the Digital Number (DN) of each pixel was transformed into a decibel (DB) utilising the following formula:

$$DB = 10 \times log_{10}|DN| \quad (1)$$

where log_{10} x represents the logarithm of u to base 10, and $|DN|$ represents the absolute value of DN.

Regarding the Landsat dataset, atmospherically corrected surface reflectance images were used through GEE (Level 2, Collection 2, Tier 1), where, for the cloud filtering, the F-mask algorithm [116] was exploited to exclude haze, clouds, shadows, and dark pixels. All the images were collected, including those with high cloud coverage, since the clouds did not cover the AoI in many cases, making the image useable. After that, the confidence interval was calculated to exclude images where the number of overlapping pixels over the AoI was lower than the confidence interval (<95%), making the measurements more reliable.

2.3.2. Interpolation and Decomposition Techniques

Missing values in the time series, which resulted from the filtering process, were interpolated using the Moving Average (M.A.) and Kalman filter algorithms to address data gaps effectively. The assessment of these two interpolation algorithms showed that the Kalman smoothing filter performed better than the M.A. filter; thus, the Kalman filter was exploited further. The Cook's distance was estimated to obtain a better insight into the effects of the filled values while analysing the time series data, which depends on the Hat matrix (H). This matrix gives a result of each value y (response value) in the data (time series) for every fitted value $\hat{y}$ created from the Kalman filter. The H trace helps to identify the factors of influence, expressing for the same observation the degree of the influence between the values (response and fitted) and the points with high leverage, which may impact the model. Generally, a value's Cook's distance exceeding three times the mean Cook's distance suggests it may be an outlier [117].

After imputing the values, a classical decomposition method was implemented for the ten VIs created from Landsat data and the VV and VH polarisation from Sentinel-1 imagery, where the VIs' formulas are indicated in Table 2. The classical decomposition method was used to separate the time-series data intro trend, seasonal, and noise components. This approach ensures that long-term patterns (trend) and periodic fluctuations (seasonality) are effectively isolated from random variations (noise), enabling a clearer analysis of vegetation changes. By applying this decomposition, we aimed to ensure that abrupt changes detected in the trend component were not influenced by short-term fluctuations or missing data imputations. This step was critical in reducing the impact of any residual interpolation effects from the Kalman filter, thereby improving the robustness of breakpoint detection. The VIs were derived through a GEE script by applying data harmonisation methods, allowing consistency and comparability within the different Landsat data.

2.3.3. BFAST Algorithm

In this study the BFAST algorithm was applied to detect abrupt changes in vegetation trends caused by dust events. The algorithm was selected for its ability to separate seasonal components, trends, and noise, making it particularly useful in long-term vegetation monitoring. To ensure robustness in detecting change points, we utilised different versions of BFAST, each serving a specific purpose in the analysis. The original BFAST algorithm was used for full time-series decomposition, allowing multiple breakpoints to be identified, while BFAST Lite was applied to improve processing efficiency and enhance sensitivity to subtle changes. Additionally, BFAST01 was employed to focus on a single major shift in the trend, reducing the likelihood of detecting minor fluctuations. These differences in sensitivity arise from their internal statistical frameworks, where BFAST Lite offers a streamlined approach to decomposition and BFAST01 is designed to capture only the most significant trend shift.

More specifically, these algorithms were implemented in the R software (v.3.3.3) through the bfast package. BFAST is a reliable algorithm for change detection, decomposing time-series data into the three elements mentioned above. This algorithm gives two options to recognise shifts, namely, to specify the numeral of breaks ("bfast"), allowing several breakpoints to be identified in a time series and to identify a significant breakpoint (function "bfast01"). The algorithm iteratively calculates the time and number of unexpected shifts, mixing the detection of changes with the additive decomposition algorithm within a data series.

Generally, the algorithm utilises a model of additive decomposition of a time series to fit a segmented linear trend and a segmented seasonal model iteratively [118,119]. The generic formula of the algorithm is expressed below.

$$Y_t = S_t + T_t + e_t,\ t = 1, 2 \ldots n \quad (2)$$

where Y_t are the data observed at time t, T_t is the trend, S_t is the data seasonality, and e_t is the remaining noise. In this formulation, the trend and seasonal components are iteratively estimated using a decomposition approach, where their contributions are dynamically adjusted based on the observed time series data. Unlike traditional regression models, BFAST does not use fixed coefficients; instead, it identifies structural changes by detecting significant shifts in the trend and seasonal components over time.

In addition to the BFAST family algorithms utilised in this study, BFAST Monitor offers an alternative approach for near-real-time detection of abrupt changes in vegetation. Unlike the original BFAST, which detects multiple breakpoints across a time series, BFAST Monitor focuses on identifying a single significant change at the end of the observation period, making it particularly suitable for operational forest monitoring [120]. Its capability

has been applied in deforestation monitoring [121], vegetation degradation [122], and ecosystem disturbances [123]. While not implemented in this study, future work could explore its potential for assessing ongoing dust-induced forest disturbances with frequent satellite acquisitions.

2.3.4. Vegetation Indices

The VIs selected for this study, presented in Table 2 below, were driven by their unique characteristics and ability to capture different aspects of vegetation health and dynamics.

Table 2. VIs assessed in the study.

No	Indicator	Formula	Reference
1	ARVI	$\frac{NIR-R-y\times(R-B)}{NIR+R-y\times(R-B)}$	[124]
2	AVI	$[NIR*(1-R)\times(NIR-R)]^{1/3}$	[125]
3	EVI	$G\times\frac{NIR-R}{NIR+C1\times R-C2\times B+L}$	[126]
4	GCI	$\frac{NIR}{G-1}$	[127]
5	MSI	$\frac{SWIR}{NIR}$	[128]
6	NDMI	$\frac{NIR-SWIR}{NIR+SWIR}$	[129]
7	NDVI	$\frac{NIR-R}{NIR+R}$	[130]
8	NDWI	$\frac{G-NIR}{G+NIR}$	[131]
9	SAVI	$\frac{NIR-R}{NIR+R+L}\times 1+L$	[132]
10	SIPI	$\frac{NIR-B}{NIR+R}$	[133]

where R = red band reflectance; G = green band reflectance; B = blue band reflectance; NIR = Near-InfraRed band reflectance; $SWIR$ = short-wave InfraRed; L = soil linearity correction factor; $C1$, $C2$ = soil adjustment factors; and y = the weight factor applied to the difference between the red and blue bands.

The Atmospherically Resistant Vegetation Index (ARVI) applies to regions with high atmospheric aerosol variations, such as Cyprus, due to the frequent extreme aerosol outbreak events like dust storms [133]. The Advanced Vegetation Index (AVI) is particularly effective in areas with sparse vegetation and significant soil exposure, such as the Paphos forest. Moreover, the Enhanced Vegetation Index (EVI) improves the vegetation signal in high biomass regions and offers improved vegetation monitoring by reducing atmospheric and canopy background influences. The Green Chlorophyll Index (GCI) estimates the content of leaf chlorophyll in various species of plants, which is helpful considering the mixed vegetation in the Paphos forest. The Moisture Stress Index (MSI) detects vegetation's moisture stress, making it appropriate for use due to the continuous water stress in Cyprus [134]. The Normalised Difference Moisture Index (NDMI) is widely known in the remote sensing field and determines the moisture in vegetation. It has also been used to detect forest disturbance [129]. The Normalised Difference Vegetation Index (NDVI) is the most widely used index, which can monitor growth and vegetation health or even identify stress or damage in vegetation [135]. The Normalised Difference Water Index (NDWI) as sensitive to the moisture levels in vegetation as NDMI and can also be utilised to monitor droughts [135]. The Soil Adjusted Vegetation Index (SAVI) is considered a modification of the NDVI with its soil brightness correction factor, providing more accurate measurements in environments with sparse vegetation. The Structure Insensitive Pigment Index measures the amount of chlorophyll and carotenoid pigment in plants without getting confused by the shape or arrangement of the leaves [136].

3. Results

As mentioned earlier, ten VIs were tested for the time-series analysis in this study, but only AVI, SAVI and EVI managed to detect forest disturbance that occurred mainly after a dust event; thus, the analysis of the optical data continues with these selected VIs. Overall, there were eight missing values in the monthly time series of the AVI, SAVI, and EVI, whereas only one missing value existed for the VH and VV polarisation. The Cook's distance was utilised to identify influential points in the time series, but despite outliers, no values were removed. Assessment of the influential points showed no significant impact on the estimated regression coefficients or the model's overall fit, ensuring the integrity of the statistical findings.

3.1. Abrupt Changes in Vegetation Dynamics

3.1.1. BFAST Original

Utilising the original BFAST algorithm, we identified two sudden changes for AVI in April 2018 and December 2019. Both breaks showed a decrease in the trend line, implying a reduction in vegetation (Figure 2a). We observed three abrupt shifts for SAVI: a decrease in August 2015 and increases in June 2019 and November 2020 (Figure 2b). Interestingly, the breaks for EVI were identical to those in SAVI, occurring on the exact dates (Figure 2c). Regarding VV polarisation, there was a single abrupt shift with a significant decrease in the backscatter coefficient in November 2015 (Figure 2d). No break was detected for the VH polarisation.

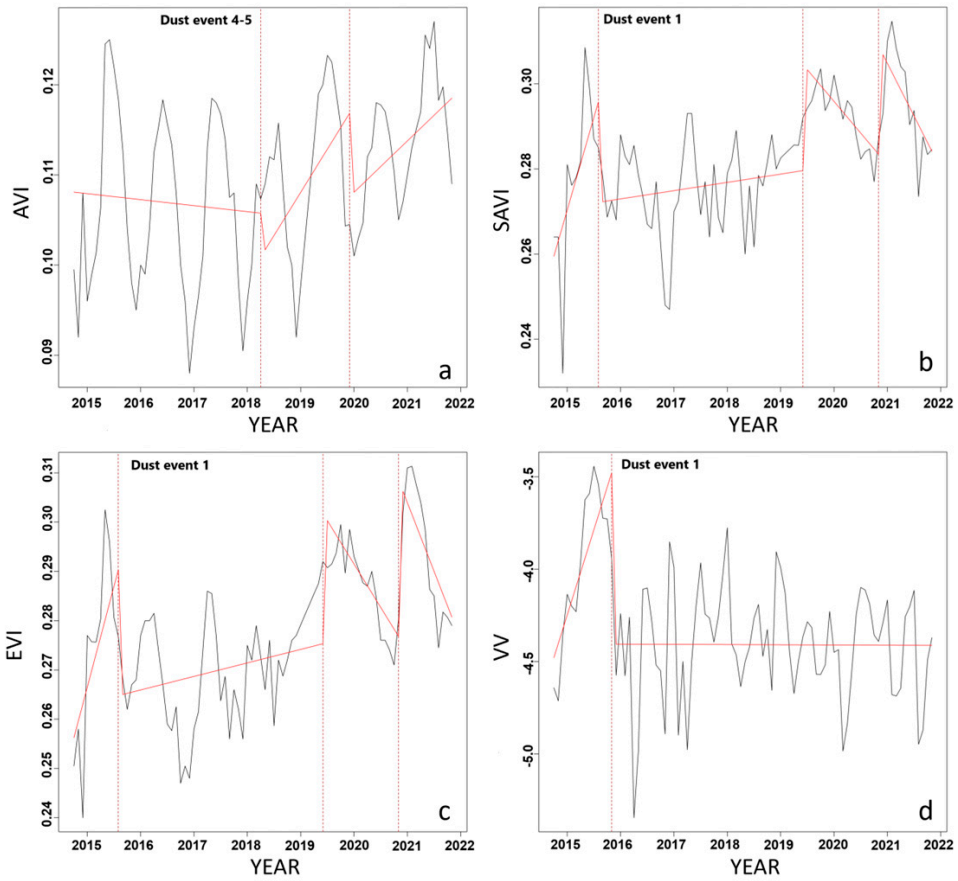

Figure 2. Detection of abrupt changes with the BFAST decomposition algorithm for AVI (**a**), SAVI (**b**), EVI (**c**), and VV polarisation (**d**). The red line indicates the breaks in the trend component. Labelled breakpoints correspond to dust events, while other detected changes may result from different environmental factors.

3.1.2. BFAST Lite

The BFAST lite algorithm detected a break in the trend of VH polarisation in October 2015 (Figure 3a) and another sudden change in the trend of VV polarisation, SAVI, and AVI in September 2015 (Figure 3b–d). These shifts indicated significant drops in the trend of the analysed polarisation and indicators, suggesting a drop in germination. Regarding EVI, three changes were identified, with the first occurring in May 2016 with a significant decrease in the trend. The second and third breaks were in May 2019 and November 2020, respectively, with both breaks showing an increase in the EVI trend, implying an increase in vegetation dynamics (Figure 3e).

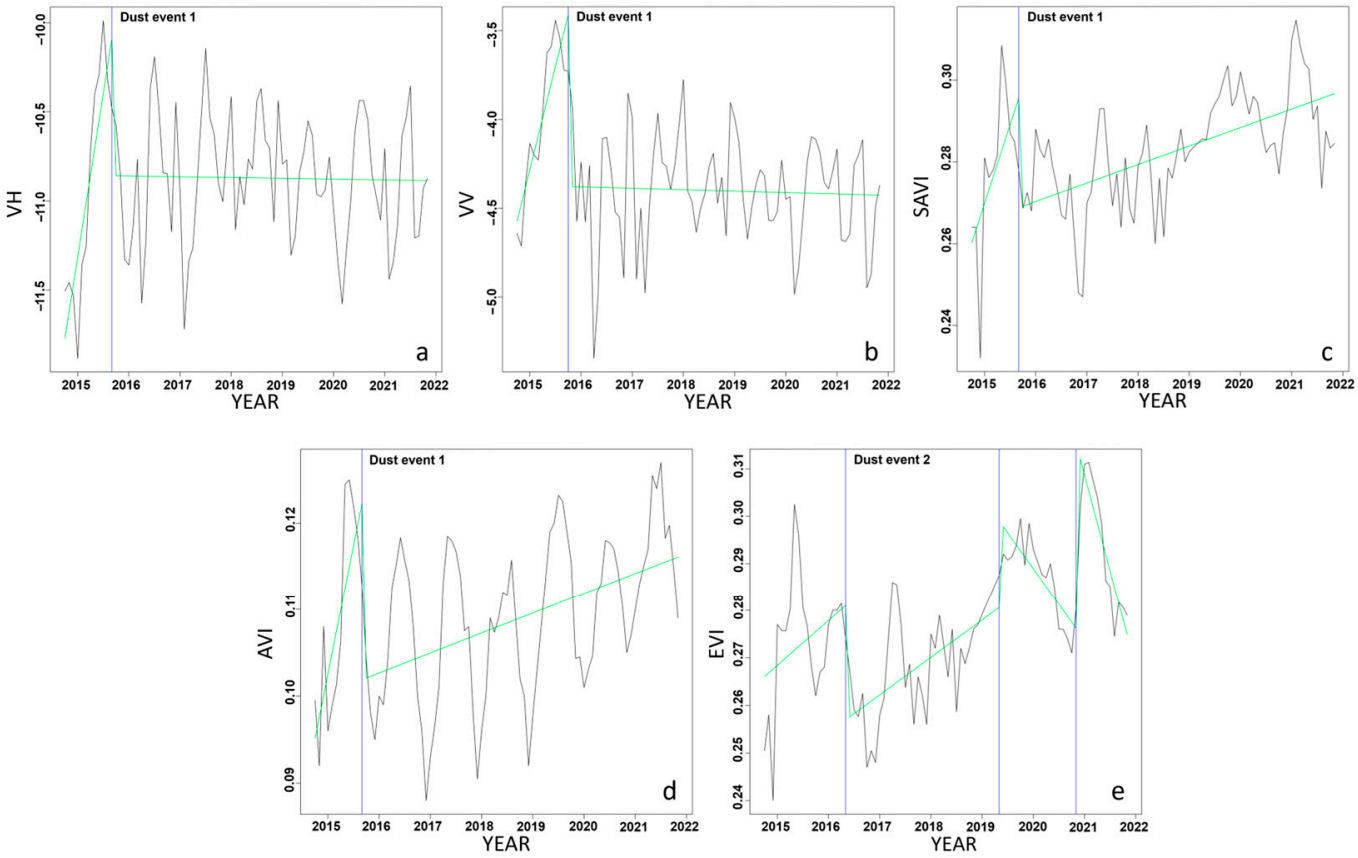

Figure 3. Detection of abrupt changes with the BFAST lite decomposition algorithm for VH (**a**), VV (**b**), SAVI (**c**), AVI polarisation (**d**), and EVI (**e**). Green and vertical blue lines indicate the breaks in the trend component. Labelled breakpoints correspond to dust events, while other detected changes may result from different environmental factors.

3.1.3. BFAST01

Applying the latest version of the BFAST algorithm, the BFAST01 algorithm showed only one abrupt change in the trend of VV polarisation in April 2018, with a slight increase in the backscatter coefficient, followed by a gradual decrease (Figure 4). No changes were detected for the VH polarisation and the three VIs.

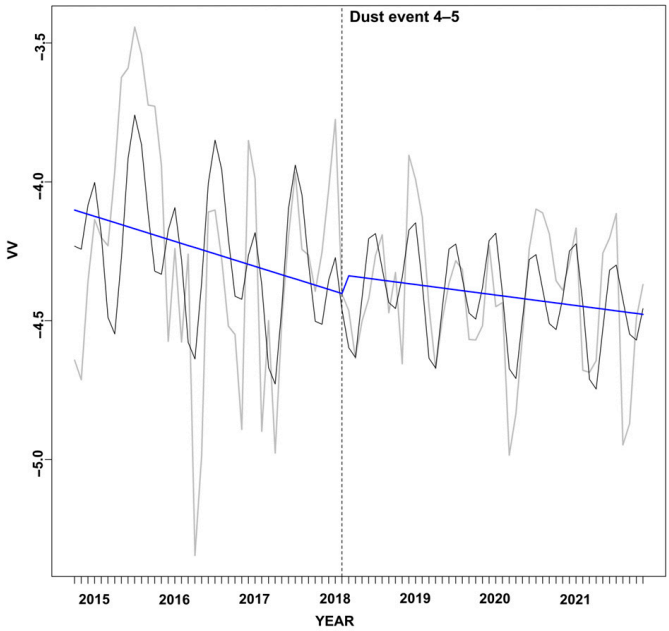

Figure 4. Detection of an abrupt change in VV polarisation with the BFAST01 decomposition algorithm. The blue line indicates the break in the trend component. Labelled breakpoints correspond to dust events.

3.2. Air Quality and Meteorological Data

Assessing PM2.5 and PM10 data from the Ayia Marina Xyliatou station (Figure A1) and the MODIS satellite (Appendix A), eight dust events were discriminated within the period 2015–2021 (Table 3). These events were classified based on elevated PM10 and PM2.5 concentrations exceeding 50 μg/m^3 and 20 μg/m^3, respectively. Rainfall data from the four meteorological stations were derived to analyse and find the duration of rainfall absence after each dust event since the lack of rain plays a critical role in vegetation's smooth functioning, as mentioned earlier. More specifically, the duration of the rainfall absence after the dust event and the amount of rainfall are indicated below in Table 3.

Table 3. Dust events over Cyprus within 2015–2019 are in chronological order, with maximum measurements of PM2.5 and PM10, including the date and amount of rainfall for the four meteorological stations in the Paphos forest.

Dust Event No	Date of Dust Event Detected by MODIS	Maximum PM2.5 Measured by the Air Quality Stations	Maximum PM10 Measured by the Air Quality Stations	Meteorological Station	Rainfall Date	SUM Precipitation (mm)	Duration of Rainfall Absence in the Days After the Maximum PM Values
1	07–12/09/2015 (Figure A2)	84.74 (08/09/2015)	478.04 (08/09/2015)	Alonoudi	20–21/09/2015	0.5	8
				Cross of Psoka	20/09/2015	1.5	
				Dodeka Anemoi		2.3	
				Finokli		24.1	
2	12/05/2016 (Figure A3)	39.33 (14/05/2016)	148.75 (14/05/2016)	Alonoudi	22–23/05/2016	0.5	10
				Cross of Psoka		2.7	
				Dodeka Anemoi	23/05/2016	1.6	11
				Finokli	22–23/05/2016	0.7	10

Table 3. *Cont.*

Dust Event No	Date of Dust Event Detected by MODIS	Maximum PM2.5 Measured by the Air Quality Stations	Maximum PM10 Measured by the Air Quality Stations	Meteorological Station	Rainfall Date	SUM Precipitation (mm)	Duration of Rainfall Absence in the Days After the Maximum PM Values
3	20–22/04/2017 (Figure A4)	11.5 (21/04/2017)	32.4 (22/04/2017)	Alonoudi	04/05/2017	44.6	12
				Cross of Psoka	17/05/2017	1.6	25
				Dodeka Anemoi	04/05/2017	19.5	12
				Finokli	17/05/2017	2.0	25
4–5	05/03/2018 22–23/03/2018 (Figure A5)	NA	NA	Alonoudi	24/03/2018	4.1	19
		15.3 (07/03/2018) 46.9–61.2 (25–26/03/2018)	50.6 (07/03/2018) 214.4–206.4 (25–26/03/2018)	Cross of Psoka		6.2	
				Dodeka Anemoi	08/03/2018	1.3	3
					24/03/2018	5.0	1
				Finokli	24/03/2018	4.3	1
6	02–04/05/2018 (Figure A6)	21.9 (05/05/2018)	74.4 (05/05/2018)	Alonoudi	07–08/05/2018	2.8	3
				Cross of Psoka	02/05/2018	0.9	0
					07–08/05/2018	11	3
				Dodeka Anemoi		4.3	3
				Finokli		13.0	3
7	18/10/2018 (Figure A7)	39.7 (18/10/2018)	159.5 (18/10/2018)	Alonoudi	NA	NA	NA
				Cross of Psoka	18–20/10/2018	8.3	0
				Dodeka Anemoi		15.6	0
				Finokli		1.1	0
8	13/04/2019 (Figure A8)	13.8 (14/04/2019)	39.1 (14/04/2019)	Alonoudi	NA	NA	NA
				Cross of Psoka	15–16/04/2019	7.1	1
				Dodeka Anemoi		2.3	
				Finokli		4.3	

4. Discussion

Evaluating the breaks produced by the BFAST algorithms, the most likely reason for the sudden changes in the trend component of the time series was due to the several dust events that occurred in the region within the study period, combined with different climatic conditions in the area and some human activities that may have changed the vegetation dynamics in the forest. Four dust events (Nos. 1, 2, 4–5, and 6) were successfully identified, as indicated in Table 4 below. While the BFAST analysis identified multiple breakpoints in the vegetation time series, only some of these could be directly linked to documented dust events. Other breakpoints may be attributed to seasonal fluctuations, precipitation anomalies, or other environmental disturbances. The observed changes in vegetation dynamics were predominantly associated with documented dust events;

however, other environmental factors may have also played a role. Vegetation responses to dust deposition are complex and may be influenced by a combination of factors, including precipitation patterns, temperature fluctuations, and soil moisture variations. For instance, prolonged drought periods or recurring dust exposure over consecutive months could lead to cumulative vegetation stress, making it difficult to attribute changes to a single dust event. Additionally, different vegetation species in the study area may exhibit varying degrees of resilience to dust-related disturbances, influencing the detectability of changes in vegetation indices. The differences in detection sensitivity between optical and radar datasets further suggest that vegetation responses may not always be immediate but can manifest over extended periods, depending on the physiological adaptations of forest species to environmental stressors.

Table 4. Identified dust events for each radar polarisation and VI per BFAST algorithm.

BFAST Original	BFAST LITE	BFAST01
SAVI 08/2015	AVI 09/2015	VV 03/2018
EVI 08/2015	VH 09/2015	
VV 11/2015	SAVI 09/2015	
AVI 04/2018	VV 10/2015	
	EVI 05/2016	

Our outcomes suggest that the trend's turning point in dust event No. 1 could be attributed to a particularly severe dust storm that originated from the deserts of northern Syria and Iraq and affected the eastern Mediterranean region from 7–12 September 2015. It is worth mentioning that 12 h before the peak of the dust event on 8 September, the concentration of dust masses reached 2000 $\mu g\ m^{-3}$ in the elevated dust layers [137]. As shown in Figure A2, MODIS and Aqua satellite images show that the dust event initiated on 7 September, maximised the next day, and faded away by 9 September. Eight days after the dust event, rainfall could have minimised the impact of dust on vegetation. However, the first radar image for this month was acquired two days before rainfall occurred, and the first optical imagery was captured during the dust event (10 September 2015), justifying the identified breaks in the graphs. Both optical (SAVI, AVI) and radar imagery (VV, VH) successfully identified this dust event, which was the largest compared to the other dust storms studied and discussed further.

Regarding dust event No. 2, only EVI successfully identified the dust event, creating a break in the graph in May 2016. This event reached high levels with 39.33 $\mu g/m^3$ and 148.75 $\mu g/m^3$ for PM2.5 and PM10, respectively. Despite MODIS detected dust particles on 12 May 2016, the in-situ measurements showed higher PM values on 14 May 2016, indicating that the dust reached the station two days after the dust event. As shown in Table 3, rainfall occurred 10 days after the peak dust levels. This delay in rainfall provided a window where dust could settle and potentially affect vegetation, allowing for observable stress without immediate interference from precipitation. However, two optical images were captured this month (7 and 23 May 2016), filtered out, and imputed utilising the Kalman filter. Since these images did not retain the original values and underwent processing to fill in missing values, the imputed data might not reflect the vegetation stress caused by dust, leading to a lack of identification. Moreover, the dust particles were detected by MODIS at night (Figure A3), meaning that the stomata of the leaves may have already closed, so the dust particles did not impact them as much. In the case of this specific dust event, while atmospheric and rainfall conditions were favourable for detection, the filtered imagery resulted in a missed opportunity to observe the event directly.

Dust event No. 3 (20–22 April 2017) was not identified by radar and optical data despite the availability of satellite images (22 and 28 April 2017 for radar and 24 April 2017 for optical) and the absence of rainfall (9 days). Although the high dust concentrations were calculated from MODIS on that day (Figure A4), the low maxima of PM 2.5 (11.5 $\mu g/m^3$) and PM 10 (32.4 $\mu g/m^3$) from the Ayia Marina Xyliatou station imply that the dust particles remained at higher altitudes rather than settling on vegetation. Additionally, interpolation of missing optical data for this period may have introduced uncertainty, reducing the likelihood of detecting dust-induced vegetation stress.

Dust events No. 4–5 (5, 22–23 March 2018) were challenging to detect due to the timing of image capture and subsequent rainfall. Optical data did not capture the event because the available Landsat images either predated the dust storms or were filtered due to cloud cover. Overall, there were three Landsat images for March 2018. The first image was captured on 2 March 2018, when the first dust storm broke out on 5 March 2018. The second image was filtered out due to clouds, while the third image was taken on 26 March 2018, when a second dust event occurred from 22 to 23 March 2018. Between the second dust storm and the 3rd Landsat image, rainfall in multiple regions (up to 6.2 mm) was observed on 24 March 2018, washing away residual dust and complicating optical imagery detection efforts. On the other hand, the radar data (VV polarisation) were successful in detection, mainly because they covered May with five observations (6, 12, 18, 24, 30 May 2018) in total, adequately covering both dust phenomena during and after their occurrence. This highlighted the advantage of frequent radar observations in minimising temporal gaps caused by missing optical data. The multiple acquired radar images with the absence of rainfall (only the "Dodeka Anemoi" meteorological station captured rainfall on the 8 March 2018) and the continued exposure of vegetation to dust particles day and night (Figure A5) before being washed away by the precipitation resulted in a unique opportunity for the radar data to effectively detect the second largest dust event of the studied period and one of the most intense episodes of African dust covering a large part of the Eastern Mediterranean [138,139].

Between 2 and 4 May 2018, dust event No. 6 (Figure A6) hit the island. This dust event reached moderate levels, with PM2.5 and PM10 peaks at 21.9 $\mu g/m^3$ and 74.4 $\mu g/m^3$, respectively. Shortly after the event (same date for Cross of Psoka and 3 days for all stations), rainfall of up to 13 mm was recorded across stations, quickly washing away dust particles and minimising their existence on vegetation (Table 3). Although both optical and radar images were captured on May 5, just as the dust event concluded, there was not enough time for the dust to cause visible or measurable stress effects on tree foliage. Consequently, while images were available, the timing and quick succession of rain prevented the dust from manifesting detectable changes in vegetation indices and polarisations. Concerning the AVI break that occurred in April 2018 (Figure 2a), a month before the May dust event, it may be related to significant rainfall in late March. During this period, multiple stations recorded substantial precipitation, with notable rainfall events on March 24 (Alonoudi: 4.1 mm, Dodeka Anemoi: 5 mm, Finokli: 4.3 mm) and heavy rainfall on March 28–29 (Alonoudi: 20, 22 mm, Dodeka Anemoi: 13.1, 50.1 mm, Finokli: 14, 23 mm) bringing soil moisture levels up considerably. While March saw substantial rainfall, precipitation was more limited throughout April before the dust event. The AVI anomaly observed in April 2018 coincided with this period of dust activity, and while dust deposition likely contributed to vegetation stress, alternative factors such as residual soil moisture from March or natural seasonal transitions may have played a role. However, given the absence of significant rainfall in the days leading up to the event and the elevated PM level recorded in the region, the likelihood of disturbance by dust being a primary driver remains high.

Another dust storm occurred on 18 October 2018 (dust event No. 7), during which the in-situ measurements from the Ayia Marina Xyliatou station showed high concentrations of PM2.5 (39.7 $\mu g/m^3$) and PM10 (159.5 $\mu g/m^3$) during the same day. However, immediate rainfall broke out on October 18–20 in Paphos forest, likely preventing dust accumulation on vegetation and limiting its detectability in remote sensing indices.

Similarly, Dust Event No. 8 occurred on 13 April 2019 (Figure A8); the in-situ measurements revealed peaks of 13.8 $\mu g/m^3$ (PM2.5) and 39.1 $\mu g/m^3$ (PM10), respectively. Although the conditions initially appeared favourable for detecting dust impacts on vegetation, there was limited rainfall one day after the dust event (Table 3), minimising the chances of observing potential dust effects. Moreover, the combination of limited optical data in April, the rainfall after the dust event, and the effect of moisture in radar signal reduced the likelihood of detecting visible dust impacts from the specific dust storm. Additionally, the relatively lower PM concentrations compared to other major dust events may have resulted in a weaker signal in both optical and radar observations. Furthermore, the lack of optical acquisitions during the critical period following the dust event meant that any potential vegetation stress might have been undetectable due to insufficient temporal coverage. This highlights the challenges associated with monitoring short-lived dust effects on forests, especially when rapid-post event rainfall further reduces their detectability in remote sensing datasets.

Overall, the radar data successfully identified only dust events Nos. 1 and 6, which were the most significant and second largest, respectively. This observation suggests that radar imagery may be more sensitive to detecting significant dust events when PM levels surpass a certain threshold. In contrast, optical data proved capable of detecting smaller dust events as well, suggesting a higher sensitivity to changes in VIs, even at lower dust concentrations. This differential detection threshold between radar and optical data highlights the potential limitations of the radar in capturing less intense dust impacts, as radar backscatter may require a more pronounced dust layer or vegetation stress to register discernible changes. In general, radar data successfully identified forest disturbances from dust only from the most intense dust events (Nos. 1 and 6).

In contrast, optical indices detected changes even for smaller events like dust event No. 2. Therefore, integrating optical and radar imageries could enhance detection sensitivity across various intensities of dust events. This integrated approach could enable a more robust assessment of dust impacts on forest ecosystems, particularly in semi-arid regions prone to frequent dust activity. While this study demonstrates the potential of Sentinel-1 SAR and Landsat data in detecting forest disturbances caused by dust events, some enhancements could improve future monitoring efforts. Integrating Machine Learning (ML) models, such as Random Forest (RF), Support Vector Machine (SVM), or Convolutional Neural Networks (CNNs), could refine the classification of dust-induced vegetation stress by distinguishing it from other disturbance factors like drought, pest infestations, or natural phenological shifts. Additional data fusion approaches that combine SAR and optical datasets (e.g., Sentinel-1, Sentinel-2 and MODIS) could improve temporal coverage, reducing data gaps due to cloud cover. Lastly, incorporating ground-based validation through field measurements (e.g., chlorophyll content, stomatal conductance) and UAVs equipped with hyperspectral sensors would enhance the accuracy of remote sensing-based dust stress detection models. These advancements could significantly improve the precision and operational efficiency of dust event monitoring in semi-arid forest ecosystems. While previous studies have examined dust storm effects on vegetation, based on our knowledge and a review of the literature, no study has utilised SAR sensors to detect the impact of dust storms on forests. Therefore, our study is the first to integrate SAR and optical time-series analysis to systematically assess forest responses to dust deposition.

The findings of this study have significant implications for forest management and conservation efforts in semi-arid regions affected by dust events. Remote sensing offers a powerful tool for monitoring vegetation stress, enabling early warning systems that can help detect potential forest decline before severe degradation occurs. By integrating satellite-based monitoring with in-situ observations, forest managers can better assess vegetation health and implement targeted interventions, such as reforestation efforts, soil stabilisation techniques, or controlled irrigation to mitigate dust-related impacts. Furthermore, understanding the role of dust deposition in vegetation stress can inform policy measures aimed at reducing anthropogenic dust sources, such as unsustainable land-use practices and deforestation. Future research should explore integration of remote sensing with ecological modelling to develop predictive frameworks for assessing long-term forest resilience under increasing dust activity and evolving climatic conditions. Additionally, further investigations at the species level could provide valuable insights into how different tree species respond to varying dust concentrations, enhancing our understanding of species-specific vulnerabilities and adaptive strategies. Moreover, future studies could benefit from a multi-sensor fusion approach, integrating Sentinel-1 SAR and Sentinel-2 (or Landsat) optical data into a unified time-series analysis. This could improve dust impact detection by leveraging SAR's ability to penetrate cloud cover and detect structural changes alongside optical sensors' sensitivity to vegetation health and pigment variations. Alternatively, the development of a hybrid radar–optical index could provide a novel metric for assessing dust-induced vegetation stress, offering a more comprehensive perspective on forest dynamics. These advancements would not only improve the precision of remote sensing applications but also provide forest managers with a more robust decision–support system for mitigating dust-related impacts on forest ecosystems.

5. Conclusions

This study demonstrates the capability of multispectral and radar satellite data to detect vegetation responses to dust events in the Paphos forest, Cyprus. Applying BFAST decomposition algorithms effectively identified several dust events, with particular sensitivity observed for the most significant ones. These results suggest that integrating SAR and optical data provides complementary insights, as radar data primarily detected the most intense dust events, while optical data captured a broader range, including those with lower PM concentrations. Our findings underscore that success depends not only on sensor capabilities but also on multiple factors, such as rainfall timing and the availability of imagery close to dust events. For instance, the immediate post-event rainfall can quickly wash dust away, minimising its impact on vegetation, while a lack of imagery near the event timeframe can reduce detection accuracy. Radar backscatter requires significant dust accumulation to register evident vegetation stress, whereas optical indices are more responsive to minor events, reflecting even subtle vegetation changes. These outcomes emphasise the importance of data integration for capturing dust impacts on vegetation under various environmental conditions. In conclusion, expanding the time series datasets and enhancing image frequency could further improve the reliability of dust event detection.

Author Contributions: Conceptualisation, C.T.; methodology, C.T.; software, C.T.; validation, C.T.; formal analysis, C.T.; investigation, C.T.; resources, C.T. and M.M.; data curation, C.T., P.K., M.M. and C.D.; writing—original draft preparation, C.T.; writing—review and editing, C.T., M.E., P.K., C.K. and D.H.; visualisation, C.T.; supervision, D.H. and I.G.; project administration, M.M.; and funding acquisition, D.H. All authors have read and agreed to the published version of the manuscript.

Funding: This work was funded by the EXCELSIOR Teaming project (Grant Agreement No. 857510, www.excelsior2020.eu, accessed on 30 January 2025).

Data Availability Statement: The original contributions presented in this study are included in the article. Further inquiries can be directed to the corresponding author.

Acknowledgments: The authors acknowledge the 'EXCELSIOR': ERATOSTHENES: Excellence Research Centre for Earth Surveillance and Space-Based Monitoring of the Environment H2020 Widespread Teaming project (www.excelsior2020.eu, accessed on 30 January 2025). The 'EXCELSIOR' project has received funding from the European Union's Horizon 2020 research and innovation programme under Grant Agreement No. 857510, from the Government of the Republic of Cyprus through the Directorate General for the European Programmes, Coordination and Development and the Cyprus University of Technology.

Conflicts of Interest: The authors declare no conflicts of interest.

Appendix A

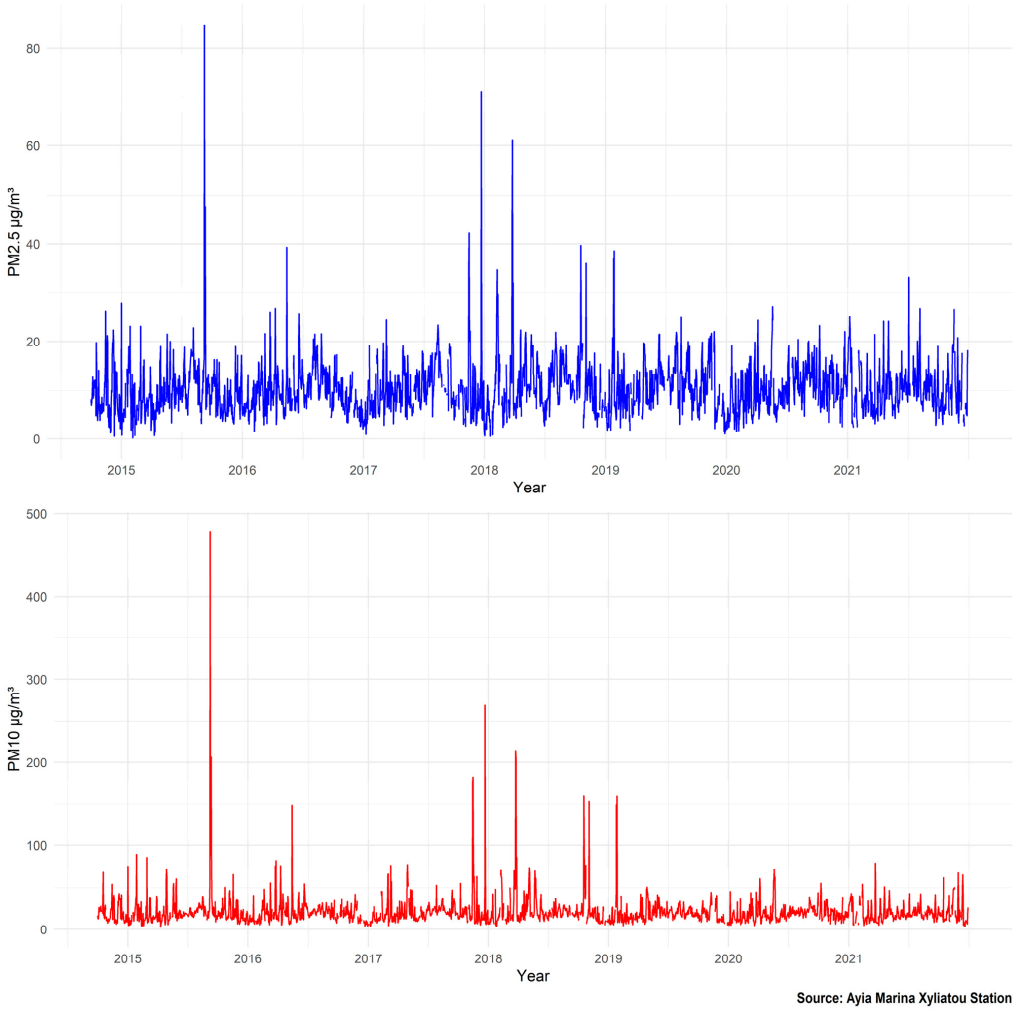

Figure A1. PM2.5 data from the Ayia Marina Xyliatou station for the period 2015–2021 (blue lines). PM10 data from the Ayia Marina Xyliatou station for the period 2015–2021 (red lines).

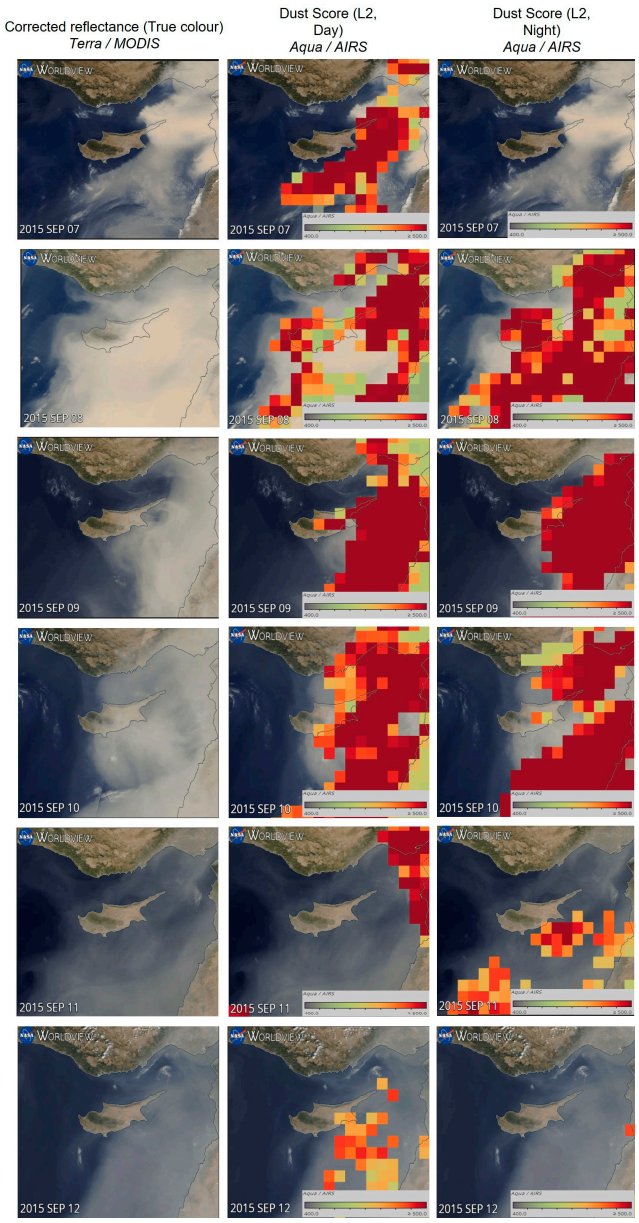

Figure A2. (**Left**) Dust storm in September 2015 in Cyprus captured by Terra–MODIS. (**Middle**) Dust score in the day (Daytime: 1:30 p.m.) as seen from the Advanced Infrared Sound (AIRS) on NASA's Aqua satellite. (**Right**) Dust score in the night (Nighttime: 1:30 a.m.).

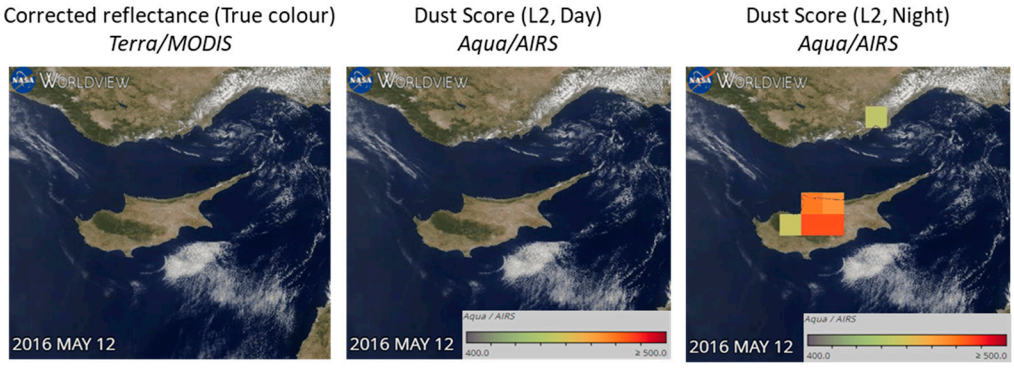

Figure A3. (**Left**) Dust storm in May 2016 in Cyprus captured by Terra–MODIS. (**Middle**) Dust score in the day (Daytime: 1:30 p.m.) as seen from the Advanced Infrared Sound (AIRS) on NASA's Aqua satellite. (**Right**) Dust score in the night (Nighttime: 1:30 a.m.).

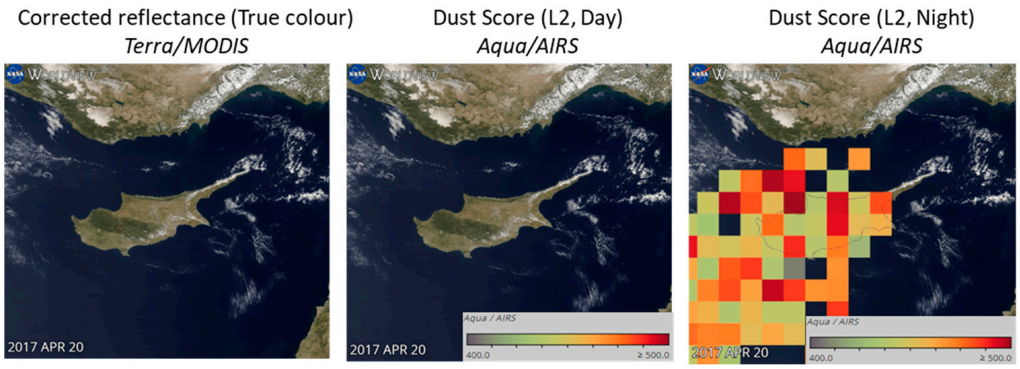

Figure A4. (**Left**) Dust storm in April 2017 in Cyprus captured by Terra–MODIS. (**Middle**) Dust score in the day (Daytime: 1:30 p.m.) as seen from the Advanced Infrared Sound (AIRS) on NASA's Aqua satellite. (**Right**) Dust score in the night (Nighttime: 1:30 a.m.).

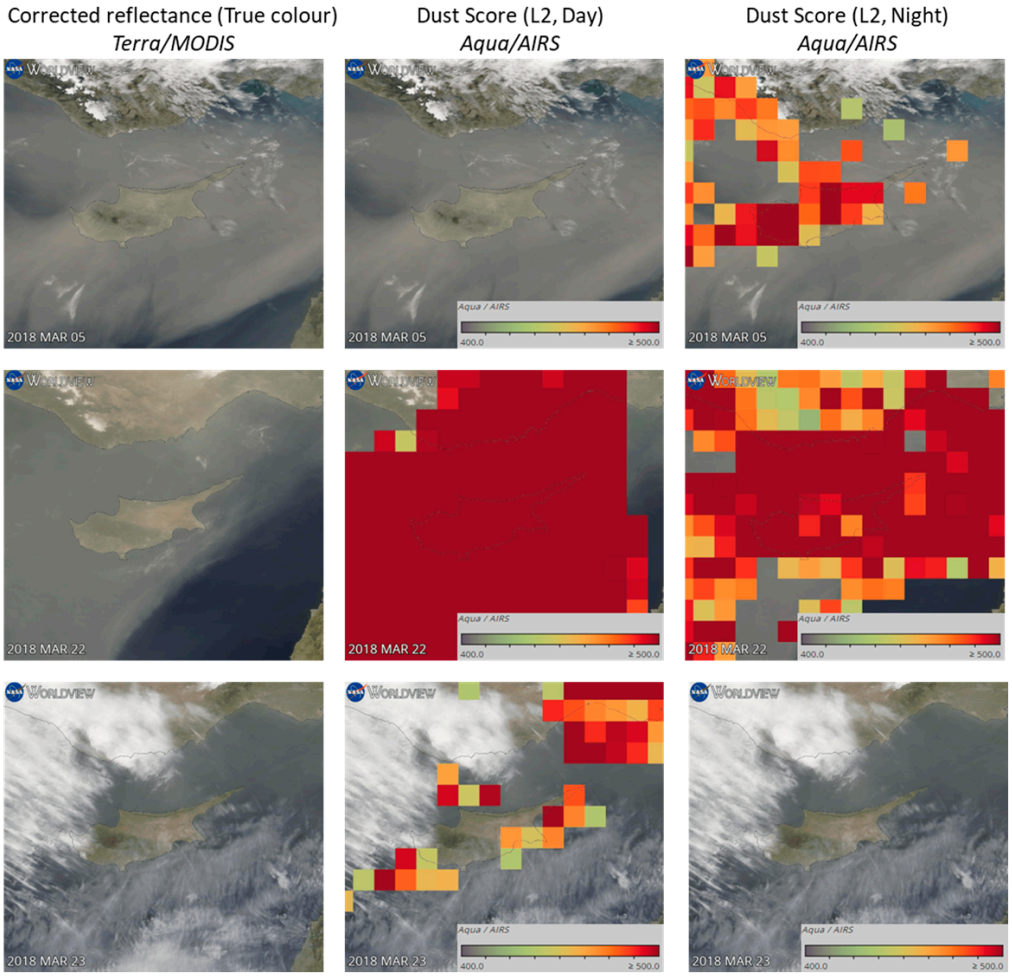

Figure A5. (**Left**) Dust storm in March 2018 in Cyprus captured by Terra–MODIS. (**Middle**) Dust score in the day (Daytime: 1:30 p.m.) as seen from the Advanced Infrared Sound (AIRS) on NASA's Aqua satellite. (**Right**) Dust score in the night (Nighttime: 1:30 a.m.).

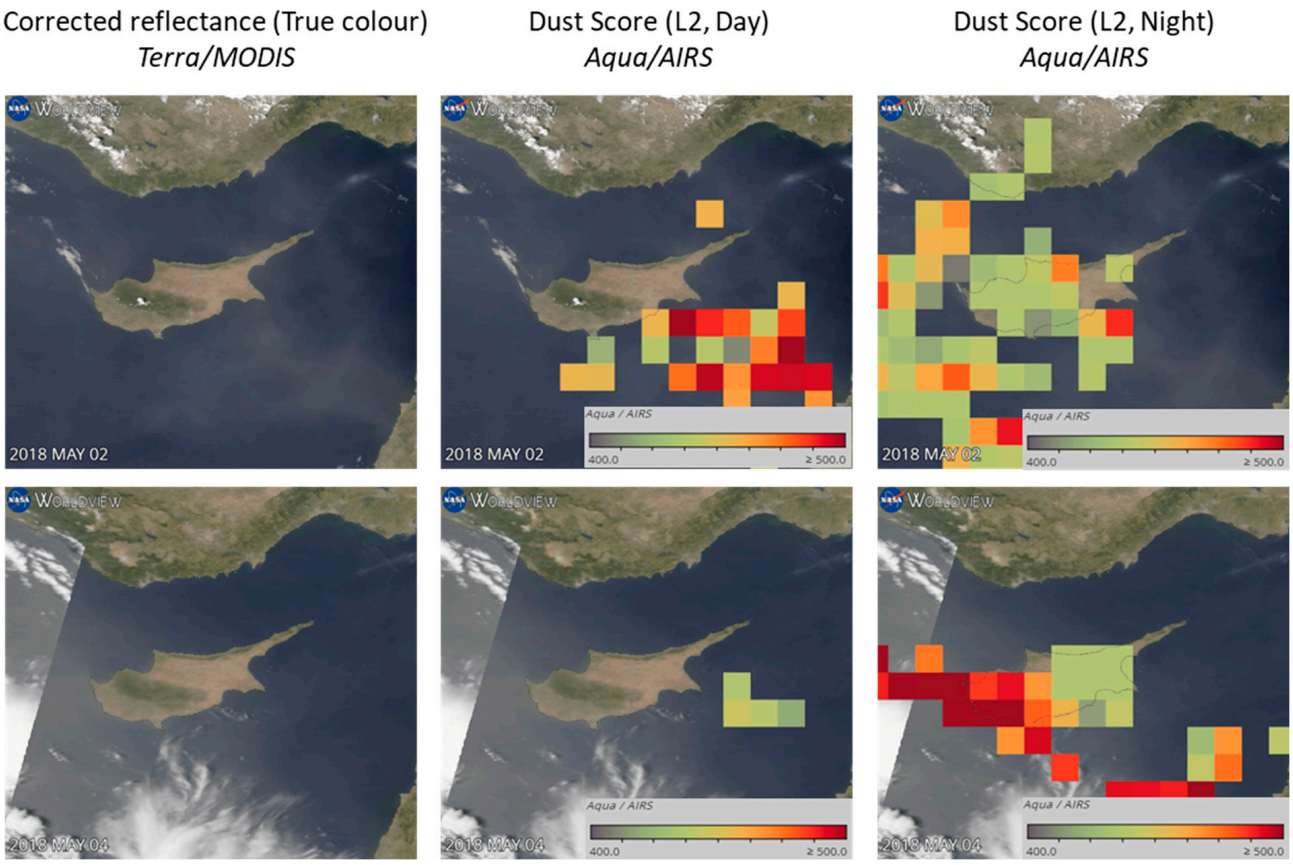

Figure A6. (**Left**) Dust storm in May 2018 in Cyprus captured by Terra–MODIS. (**Middle**) Dust score in the day (Daytime: 1:30 p.m.) as seen from the Advanced Infrared Sound (AIRS) on NASA's Aqua satellite. (**Right**) Dust score in the night (Nighttime: 1:30 a.m.).

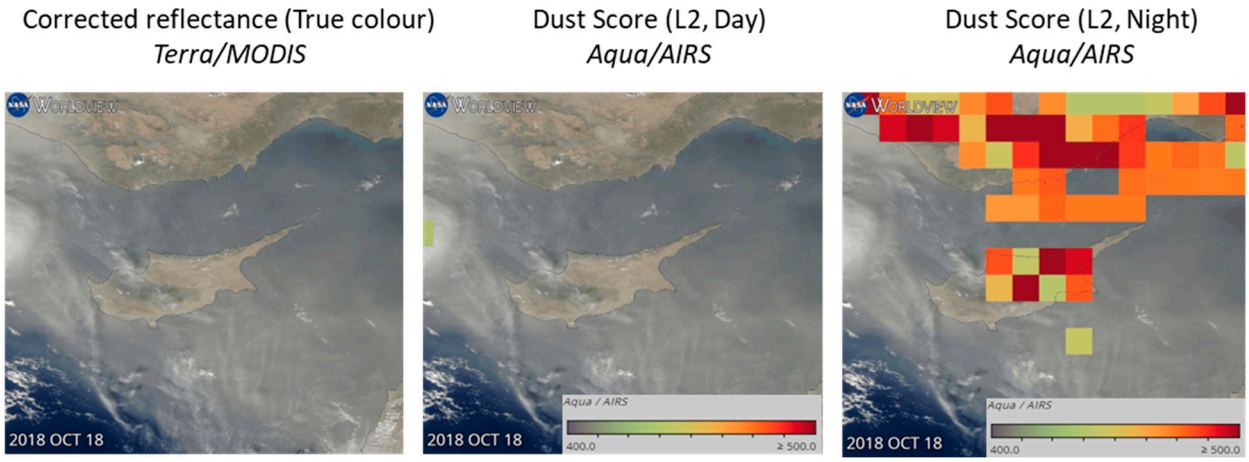

Figure A7. (**Left**) Dust storm in October 2018 in Cyprus captured by Terra–MODIS. (**Middle**) Dust score in the day (Daytime: 1:30 p.m.) as seen from the Advanced Infrared Sound (AIRS) on NASA's Aqua satellite. (**Right**) Dust score in the night (Nighttime: 1:30 a.m.).

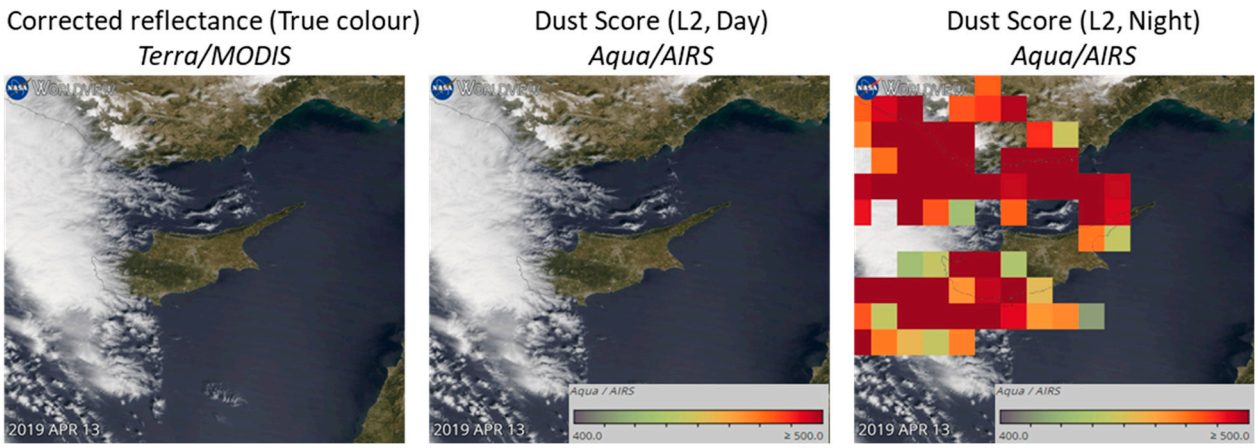

Figure A8. (**Left**) Dust storm in April 2019 in Cyprus captured by Terra–MODIS. (**Middle**) Dust score in the day (Daytime: 1:30 p.m.) as seen from the Advanced Infrared Sound (AIRS) on NASA's Aqua satellite. (**Right**) Dust score in the night (Nighttime: 1:30 a.m.).

References

1. Dar, M.A.; Ahmed, R.; Latif, M.; Azam, M. Climatology of Dust Storm Frequency and Its Association with Temperature and Precipitation Patterns over Pakistan. *Nat. Hazards* **2022**, *110*, 655–677. [CrossRef]
2. Toth, J.R., III; Rajupet, S.; Squire, H.; Volbers, B.; Zhou, J.; Xie, L.; Sankaran, R.M.; Lacks, D.J. Electrostatic Forces Alter Particle Size Distributions in Atmospheric Dust. *Atmos. Chem. Phys.* **2020**, *20*, 3181–3190. [CrossRef]
3. Darvishi Boloorani, A.; Soleimani, M.; Papi, R.; Neysani Samany, N.; Teymouri, P.; Soleimani, Z. Sources, Drivers, and Impacts of Sand and Dust Storms: A Global View. In *Dust and Health: Challenges and Solutions*; Springer: Berlin/Heidelberg, Germany, 2023; pp. 31–49.
4. African Union Commission. *The Sustainable Forest Management Framework for Africa (2020–2030)*; African Union Commission: Addis Ababa, Ethiopia, 2020; p. 32.
5. Nair, C.T.S.; Rutt, R. Creating Forestry Jobs to Boost the Economy and Build a Green Future. *Unasylva* **2009**, *233*, 3–10.
6. IUCN. Forest and Climate Change, IUCN Issues in Brief 2015. Available online: https://iucn.org/sites/default/files/import/downloads/forests_and_climate_change_issues_brief_cop21_011215.pdf (accessed on 26 February 2025).
7. Olander, L.P.; Gibbs, H.K.; Steininger, M.; Swenson, J.J.; Murray, B.C. Reference Scenarios for Deforestation and Forest Degradation in Support of REDD: A Review of Data and Methods. *Environ. Res. Lett.* **2008**, *3*, 25011. [CrossRef]
8. van der Werf, G.R.; Morton, D.C.; DeFries, R.S.; Olivier, J.G.J.; Kasibhatla, P.S.; Jackson, R.B.; Collatz, G.J.; Randerson, J.T. CO_2 Emissions from Forest Loss. *Nat. Geosci.* **2009**, *2*, 737–738. [CrossRef]
9. Gibbs, H.K.; Brown, S.; Niles, J.O.; Foley, J.A. Monitoring and Estimating Tropical Forest Carbon Stocks: Making REDD a Reality. *Environ. Res. Lett.* **2007**, *2*, 45023. [CrossRef]
10. FAO. *Global Forest Resources Assessment 2010 Main Report FAO Working Paper 144/E*; Food and Agriculture Organization (FAO) of the United Nations (UN): Rome, Italy, 2010.
11. Stanturf, J.A.; Palik, B.J.; Dumroese, R.K. Contemporary Forest Restoration: A Review Emphasizing Function. *For. Ecol. Manag.* **2014**, *331*, 292–323. [CrossRef]
12. Sasaki, N.; Putz, F.E. Critical Need for New Definitions of "Forest" and "Forest Degradation" in Global Climate Change Agreements. *Conserv. Lett.* **2009**, *2*, 226–232. [CrossRef]
13. Thompson, I.D.; Guariguata, M.R.; Okabe, K.; Bahamondez, C.; Nasi, R.; Heymell, V.; Sabogal, C. An Operational Framework for Defining and Monitoring Forest Degradation. *Ecol. Soc.* **2013**, *18*, 20. [CrossRef]
14. Ahrends, A.; Burgess, N.D.; Milledge, S.A.H.; Bulling, M.T.; Fisher, B.; Smart, J.C.R.; Clarke, G.P.; Mhoro, B.E.; Lewis, S.L. Predictable Waves of Sequential Forest Degradation and Biodiversity Loss Spreading from an African City. *Proc. Natl. Acad. Sci. USA* **2010**, *107*, 14556–14561. [CrossRef]
15. Chazdon, R.L. Beyond Deforestation: Restoring Forests and Ecosystem Services on Degraded Lands. *Science* **2008**, *320*, 1458–1460. [CrossRef]
16. Hosonuma, N.; Herold, M.; De Sy, V.; De Fries, R.S.; Brockhaus, M.; Verchot, L.; Angelsen, A.; Romijn, E. An Assessment of Deforestation and Forest Degradation Drivers in Developing Countries. *Environ. Res. Lett.* **2012**, *7*, 044009. [CrossRef]
17. Mon, M.S.; Mizoue, N.; Htun, N.Z.; Kajisa, T.; Yoshida, S. Factors Affecting Deforestation and Forest Degradation in Selectively Logged Production Forest: A Case Study in Myanmar. *For. Ecol. Manag.* **2012**, *267*, 190–198. [CrossRef]

18. Prodromou, M.; Gitas, I.; Themistocleous, K.; Danezis, C.; Ambrosia, V.; Hadjimitsis, D. The Use of Sentinel-2 Satellite Data for Burn Severity Mapping for Arakapas Fire Event in Cyprus. In Proceedings of the IGARSS 2023—2023 IEEE International Geoscience and Remote Sensing Symposium, Pasadena, CA, USA, 16 July 2023; pp. 2556–2559.
19. Caballero Espejo, J.; Messinger, M.; Román-Dañobeytia, F.; Ascorra, C.; Fernandez, L.; Silman, M. Deforestation and Forest Degradation Due to Gold Mining in the Peruvian Amazon: A 34-Year Perspective. *Remote Sens.* **2018**, *10*, 1903. [CrossRef]
20. Asner, G.P.; Jones, M.O.; Martin, R.E.; Knapp, D.E.; Hughes, R.F. Remote Sensing of Native and Invasive Species in Hawaiian Forests. *Remote Sens. Environ.* **2008**, *112*, 1912–1926. [CrossRef]
21. Meng, R.; Gao, R.; Zhao, F.; Huang, C.; Sun, R.; Lv, Z.; Huang, Z. Landsat-Based Monitoring of Southern Pine Beetle Infestation Severity and Severity Change in a Temperate Mixed Forest. *Remote Sens. Environ.* **2022**, *269*, 112847. [CrossRef]
22. Anna, C. New EU Forest Strategy for 2030. 2022. Available online: https://www.europarl.europa.eu/RegData/etudes/ATAG/2022/698936/EPRS_ATA(2022)698936_EN.pdf (accessed on 26 February 2025).
23. Da Silva-Pinheiro, J.; Lins, L.; Souza, F.C.; da Silva, C.E.M.; Moura, F.D.B.P.; Endres, L.; Justino, G.C. Drought-Stress Tolerance in Three Semi-Arid Species Used to Recover Logged Areas. *Braz. J. Bot.* **2016**, *39*, 1031–1038. [CrossRef]
24. Peñuelas, J.; Filella, I.; Zhang, X.; Llorens, L.; Ogaya, R.; Lloret, F.; Comas, P.; Estiarte, M.; Terradas, J. Complex Spatiotemporal Phenological Shifts as a Response to Rainfall Changes. *New Phytol.* **2004**, *161*, 837–846. [CrossRef]
25. Suepa, T.; Qi, J.; Lawawirojwong, S.; Messina, J.P. Understanding Spatio-Temporal Variation of Vegetation Phenology and Rainfall Seasonality in the Monsoon Southeast Asia. *Environ. Res.* **2016**, *147*, 621–629. [CrossRef]
26. Barrett, A.; Brown, L. Effects of Rainfall, Temperature and Photoperiod on the Phenology of Ephemeral Resources for Selected Bushveld Woody Plant Species in Southern Africa. *PLoS ONE* **2021**, *16*, e0251421. [CrossRef]
27. Cleland, E.; Chuine, I.; Menzel, A.; Mooney, H.; Schwartz, M. Shifting Plant Phenology in Response to Global Change. *Trends Ecol. Evol.* **2007**, *22*, 357–365. [CrossRef] [PubMed]
28. Walker, W.H.; Meléndez-Fernández, O.H.; Nelson, R.J.; Reiter, R.J. Global Climate Change and Invariable Photoperiods: A Mismatch That Jeopardizes Animal Fitness. *Ecol. Evol.* **2019**, *9*, 10044–10054. [CrossRef]
29. Meng, L.; Zhou, Y.; Gu, L.; Richardson, A.D.; Peñuelas, J.; Fu, Y.; Wang, Y.; Asrar, G.R.; De Boeck, H.J.; Mao, J. Photoperiod Decelerates the Advance of Spring Phenology of Six Deciduous Tree Species under Climate Warming. *Glob. Change Biol.* **2021**, *27*, 2914–2927. [CrossRef] [PubMed]
30. Zhou, X.; Geng, X.; Yin, G.; Hänninen, H.; Hao, F.; Zhang, X.; Fu, Y.H. Legacy Effect of Spring Phenology on Vegetation Growth in Temperate China. *Agric. For. Meteorol.* **2020**, *281*, 107845. [CrossRef]
31. Fan, B.; Guo, L.; Li, N.; Chen, J.; Lin, H.; Zhang, X.; Shen, M.; Rao, Y.; Wang, C.; Ma, L. Earlier Vegetation Green-up Has Reduced Spring Dust Storms. *Sci. Rep.* **2014**, *4*, 6749. [CrossRef]
32. Jeong, S.-J.; Ho, C.-H.; Choi, S.-D.; Kim, J.; Lee, E.-J.; Gim, H.-J. Satellite Data-Based Phenological Evaluation of the Nationwide Reforestation of South Korea. *PLoS ONE* **2013**, *8*, e58900. [CrossRef] [PubMed]
33. Liu, Q.; Piao, S.; Janssens, I.A.; Fu, Y.; Peng, S.; Lian, X.; Ciais, P.; Myneni, R.B.; Peñuelas, J.; Wang, T. Extension of the Growing Season Increases Vegetation Exposure to Frost. *Nat. Commun.* **2018**, *9*, 426. [CrossRef]
34. Menzel, A.; Yuan, Y.; Matiu, M.; Sparks, T.; Scheifinger, H.; Gehrig, R.; Estrella, N. Climate Change Fingerprints in Recent European Plant Phenology. *Glob. Change Biol.* **2020**, *26*, 2599–2612. [CrossRef]
35. Miltiadou, M.; Antoniou, E.; Theocharidis, C.; Danezis, C. Do People Understand and Observe the Effects of Climate Crisis on Forests? The Case Study of Cyprus. *Forests* **2021**, *12*, 1152. [CrossRef]
36. Wolkovich, E.M.; Cook, B.I.; Davies, T.J. Progress towards an Interdisciplinary Science of Plant Phenology: Building Predictions across Space, Time and Species Diversity. *New Phytol.* **2014**, *201*, 1156–1162. [CrossRef]
37. Buitenwerf, R.; Rose, L.; Higgins, S.I. Three Decades of Multi-Dimensional Change in Global Leaf Phenology. *Nat. Clim. Chang.* **2015**, *5*, 364–368. [CrossRef]
38. Johansson, J.; Kristensen, N.P.; Nilsson, J.; Jonzén, N. The Eco-evolutionary Consequences of Interspecific Phenological Asynchrony—A Theoretical Perspective. *Oikos* **2015**, *124*, 102–112. [CrossRef]
39. Baghzouz, M.; Devitt, D.A.; Fenstermaker, L.F.; Young, M.H. Monitoring Vegetation Phenological Cycles in Two Different Semi-Arid Environmental Settings Using a Ground-Based NDVI System: A Potential Approach to Improve Satellite Data Interpretation. *Remote Sens.* **2010**, *2*, 990–1013. [CrossRef]
40. Zheng, H.; Cheng, T.; Yao, X.; Deng, X.; Tian, Y.; Cao, W.; Zhu, Y. Detection of Rice Phenology through Time Series Analysis of Ground-Based Spectral Index Data. *Field Crops Res.* **2016**, *198*, 131–139. [CrossRef]
41. Inoue, T.; Nagai, S.; Kobayashi, H.; Koizumi, H. Utilization of Ground-Based Digital Photography for the Evaluation of Seasonal Changes in the Aboveground Green Biomass and Foliage Phenology in a Grassland Ecosystem. *Ecol. Inform.* **2015**, *25*, 1–9. [CrossRef]
42. Richardson, A.D.; Hufkens, K.; Milliman, T.; Aubrecht, D.M.; Chen, M.; Gray, J.M.; Johnston, M.R.; Keenan, T.F.; Klosterman, S.T.; Kosmala, M.; et al. Tracking Vegetation Phenology across Diverse North American Biomes Using PhenoCam Imagery. *Sci. Data* **2018**, *5*, 180028. [CrossRef] [PubMed]

43. Luo, Y.; El-Madany, T.S.; Filippa, G.; Ma, X.; Ahrens, B.; Carrara, A.; Gonzalez-Cascon, R.; Cremonese, E.; Galvagno, M.; Hammer, T.W. Using Near-Infrared-Enabled Digital Repeat Photography to Track Structural and Physiological Phenology in Mediterranean Tree–Grass Ecosystems. *Remote Sens.* **2018**, *10*, 1293. [CrossRef]
44. Reed, B.C.; Schwartz, M.D.; Xiao, X. Remote Sensing Phenology. In *Phenology of Ecosystem Processes*; Springer: Berlin/Heidelberg, Germany, 2009; pp. 231–246.
45. Pastor-Guzman, J.; Dash, J.; Atkinson, P.M. Remote Sensing of Mangrove Forest Phenology and Its Environmental Drivers. *Remote Sens. Environ.* **2018**, *205*, 71–84. [CrossRef]
46. Weber, M.; Hao, D.; Asrar, G.R.; Zhou, Y.; Li, X.; Chen, M. Exploring the Use of DSCOVR/EPIC Satellite Observations to Monitor Vegetation Phenology. *Remote Sens.* **2020**, *12*, 2384. [CrossRef]
47. Eliades, M.; Michaelides, S.; Evagorou, E.; Fotiou, K.; Fragkos, K.; Leventis, G.; Theocharidis, C.; Panagiotou, C.F.; Mavrovouniotis, M.; Neophytides, S.; et al. Earth Observation in the EMMENA Region: Scoping Review of Current Applications and Knowledge Gaps. *Remote Sens.* **2023**, *15*, 4202. [CrossRef]
48. Cunha, M.; Marçal, A.R.S.; Rodrigues, A. A Comparative Study of Satellite and Ground-Based Vineyard Phenology. In Proceedings of the 29th Symposium of the European Association of Remote Sensing Laboratories, Chania, Greece, 15 March 2010; pp. 68–77.
49. Hmimina, G.; Dufrêne, E.; Pontailler, J.-Y.; Delpierre, N.; Aubinet, M.; Caquet, B.; De Grandcourt, A.; Burban, B.; Flechard, C.; Granier, A. Evaluation of the Potential of MODIS Satellite Data to Predict Vegetation Phenology in Different Biomes: An Investigation Using Ground-Based NDVI Measurements. *Remote Sens. Environ.* **2013**, *132*, 145–158. [CrossRef]
50. Nezval, O.; Krejza, J.; Světlík, J.; Šigut, L.; Horáček, P. Comparison of Traditional Ground-Based Observations and Digital Remote Sensing of Phenological Transitions in a Floodplain Forest. *Agric. For. Meteorol.* **2020**, *291*, 108079. [CrossRef]
51. Wang, S.; Yang, B.; Yang, Q.; Lu, L.; Wang, X.; Peng, Y. Temporal Trends and Spatial Variability of Vegetation Phenology over the Northern Hemisphere during 1982–2012. *PLoS ONE* **2016**, *11*, e0157134. [CrossRef] [PubMed]
52. Tian, J.; Zhu, X.; Wu, J.; Shen, M.; Chen, J. Coarse-Resolution Satellite Images Overestimate Urbanization Effects on Vegetation Spring Phenology. *Remote Sens.* **2020**, *12*, 117. [CrossRef]
53. Wu, S.; Wang, J.; Yan, Z.; Song, G.; Chen, Y.; Ma, Q.; Deng, M.; Wu, Y.; Zhao, Y.; Guo, Z. Monitoring Tree-Crown Scale Autumn Leaf Phenology in a Temperate Forest with an Integration of PlanetScope and Drone Remote Sensing Observations. *ISPRS J. Photogramm. Remote Sens.* **2021**, *171*, 36–48. [CrossRef]
54. Theocharidis, C.; Eliades, M.; Gitas, I.; Papoutsa, C.; Kontoes, C.; Christofe, A.; Danezis, C.; Hadjimitsis, D. What Do Long-Term Satellite Data Reveal about Forest Dynamics in the Paphos Forest? In Proceedings of the IGARSS 2024—2024 IEEE International Geoscience and Remote Sensing Symposium, Athens, Greece, 7 July 2024; pp. 3650–3654.
55. Theocharidis, C.; Eliades, M.; Gitas, I.; Danezis, C.; Hadjimitsis, D. Monitoring Forest Dynamics between 1987-2023: An NDVI Analysis of Three Dominant Species in Paphos Forest, Cyprus. In Proceedings of the Tenth International Conference on Remote Sensing and Geoinformation of the Environment (RSCy2024), Paphos, Cyprus, 8–9 April 2024; Michaelides, S.C., Hadjimitsis, D.G., Danezis, C., Kyriakides, N., Christofe, A., Themistocleous, K., Schreier, G., Eds.; SPIE: Bellingham, WA, USA, 2024; p. 13.
56. Song, Y.; Wang, J. Mapping Winter Wheat Planting Area and Monitoring Its Phenology Using Sentinel-1 Backscatter Time Series. *Remote Sens.* **2019**, *11*, 449. [CrossRef]
57. McNairn, H.; Jiao, X.; Pacheco, A.; Sinha, A.; Tan, W.; Li, Y. Estimating Canola Phenology Using Synthetic Aperture Radar. *Remote Sens. Environ.* **2018**, *219*, 196–205. [CrossRef]
58. Wang, H.; Magagi, R.; Goïta, K.; Trudel, M.; McNairn, H.; Powers, J. Crop Phenology Retrieval via Polarimetric SAR Decomposition and Random Forest Algorithm. *Remote Sens. Environ.* **2019**, *231*, 111234. [CrossRef]
59. Bargiel, D. A New Method for Crop Classification Combining Time Series of Radar Images and Crop Phenology Information. *Remote Sens. Environ.* **2017**, *198*, 369–383. [CrossRef]
60. Simonson, W.; Allen, H.; Coomes, D. Effect of Tree Phenology on LiDAR Measurement of Mediterranean Forest Structure. *Remote Sens.* **2018**, *10*, 659. [CrossRef]
61. Salas, E.A.L. Waveform LiDAR Concepts and Applications for Potential Vegetation Phenology Monitoring and Modeling: A Comprehensive Review. *Geo-Spat. Inf. Sci.* **2021**, *24*, 179–200. [CrossRef]
62. Berra, E.F.; Gaulton, R.; Barr, S. Use of a Digital Camera Onboard a UAV to Monitor Spring Phenology at Individual Tree Level. In Proceedings of the 2016 IEEE International Geoscience and Remote Sensing Symposium (IGARSS), Beijing, China, 10–15 July 2016; pp. 3496–3499.
63. D'Odorico, P.; Besik, A.; Wong, C.Y.S.; Isabel, N.; Ensminger, I. High-throughput Drone-based Remote Sensing Reliably Tracks Phenology in Thousands of Conifer Seedlings. *New Phytol.* **2020**, *226*, 1667–1681. [CrossRef] [PubMed]
64. Van Iersel, W.K.; Straatsma, M.W.; Addink, E.A.; Middelkoop, H. Monitoring Phenology of Floodplain Grassland and Herbaceous Vegetation with UAV Imagery. *Int. Soc. Photogramm. Remote Sens.* **2016**, *41*, 569–571.
65. Berra, E.F.; Gaulton, R.; Barr, S. Assessing Spring Phenology of a Temperate Woodland: A Multiscale Comparison of Ground, Unmanned Aerial Vehicle and Landsat Satellite Observations. *Remote Sens. Environ.* **2019**, *223*, 229–242. [CrossRef]

66. Stendardi, L.; Karlsen, S.; Niedrist, G.; Gerdol, R.; Zebisch, M.; Rossi, M.; Notarnicola, C. Exploiting Time Series of Sentinel-1 and Sentinel-2 Imagery to Detect Meadow Phenology in Mountain Regions. *Remote Sens.* **2019**, *11*, 542. [CrossRef]
67. Meroni, M.; d'Andrimont, R.; Vrieling, A.; Fasbender, D.; Lemoine, G.; Rembold, F.; Seguini, L.; Verhegghen, A. Comparing Land Surface Phenology of Major European Crops as Derived from SAR and Multispectral Data of Sentinel-1 and-2. *Remote Sens. Environ.* **2021**, *253*, 112232. [CrossRef] [PubMed]
68. Yang, Z.; Shao, Y.; Li, K.; Liu, Q.; Liu, L.; Brisco, B. An Improved Scheme for Rice Phenology Estimation Based on Time-Series Multispectral HJ-1A/B and Polarimetric RADARSAT-2 Data. *Remote Sens. Environ.* **2017**, *195*, 184–201. [CrossRef]
69. Coletta, A.; Battagliere, M.L.; Virelli, M. Observation from Space: SAR Systems. In *Encyclopedic Atlas of Terrestrial Impact Craters*; Springer: Berlin/Heidelberg, Germany, 2019; pp. 41–50.
70. Theocharidis, C.; Gitas, I.; Danezis, C.; Hadjimitsis, D. *Satellite Times-Series Analysis and Assessment of the BFAST Algorithm to Detect Possible Abrupt Changes in Forest Seasonality Utilising Sentinel-1 and Sentinel-2 Data. Case Study: Paphos Forest, Cyprus*; Copernicus Meetings: Valencia, Spain, 2023.
71. Miltiadou, M.; Theocharidis, C.; Karathanassi, V.; Agapiou, A.; Nikolaidis, M.; Danezis, C. Understanding Phenological Changes of Coniferous Forests in Cyprus Using Time-Series of SAR Data from 2015 till 2020. In Proceedings of the SilviLaser 2021, Vienna, Austria, 28–30 September 2021; p. 3.
72. Gao, Y.; Yun, T.; Chen, B.; Lai, H.; Wang, X.; Wang, G.; Wang, X.; Wu, Z.; Kou, W. Improving the Accuracy of Canopy Height Mapping in Rubber Plantations Based on Stand Age, Multi-Source Satellite Images, and Random Forest Algorithm. *Int. J. Appl. Earth Obs. Geoinf.* **2024**, *131*, 103941. [CrossRef]
73. Soheili, F.; Woodward, S.; Abdul-Hamid, H.; Naji, H.R. The Effect of Dust Deposition on the Morphology and Physiology of Tree Foliage. *Water Air Soil Pollut.* **2023**, *234*, 339. [CrossRef]
74. Namdari, S.; Zghair Alnasrawi, A.I.; Ghorbanzadeh, O.; Sorooshian, A.; Kamran, K.V.; Ghamisi, P. Time Series of Remote Sensing Data for Interaction Analysis of the Vegetation Coverage and Dust Activity in the Middle East. *Remote Sens.* **2022**, *14*, 2963. [CrossRef]
75. Mao, R.; Ho, C.-H.; Feng, S.; Gong, D.-Y.; Shao, Y. The Influence of Vegetation Variation on Northeast Asian Dust Activity. *Asia-Pac. J. Atmos. Sci.* **2013**, *49*, 87–94. [CrossRef]
76. Sun, X.; Yuan, L.; Liu, M.; Liang, S.; Li, D.; Liu, L. Quantitative Estimation for the Impact of Mining Activities on Vegetation Phenology and Identifying Its Controlling Factors from Sentinel-2 Time Series. *Int. J. Appl. Earth Obs. Geoinf.* **2022**, *111*, 102814. [CrossRef]
77. Kayet, N.; Pathak, K.; Chakrabarty, A.; Singh, C.P.; Chowdary, V.M.; Kumar, S.; Sahoo, S. Forest Health Assessment for Geo-Environmental Planning and Management in Hilltop Mining Areas Using Hyperion and Landsat Data. *Ecol. Indic.* **2019**, *106*, 105471. [CrossRef]
78. Hamzeh, N.H.; Kaskaoutis, D.G.; Rashki, A.; Mohammadpour, K. Long-Term Variability of Dust Events in Southwestern Iran and Its Relationship with the Drought. *Atmosphere* **2021**, *12*, 1350. [CrossRef]
79. Sofue, Y.; Hoshino, B.; Demura, Y.; Kai, K.; Baba, K.; Nduati, E.; Kondoh, A.; Sternberg, T. Satellite Monitoring of Vegetation Response to Precipitation and Dust Storm Outbreaks in Gobi Desert Regions. *Land* **2018**, *7*, 19. [CrossRef]
80. Moradi, A.; Taheri Abkenar, K.; Afshar Mohammadian, M.; Shabanian, N. Effects of Dust on Forest Tree Health in Zagros Oak Forests. *Environ. Monit. Assess.* **2017**, *189*, 549. [CrossRef]
81. Javanmard, Z.; Tabari Kouchaksaraei, M.; Bahrami, H.A.; Hosseini, S.M.; Modarres Sanavi, S.A.M.; Struve, D.; Ammere, C. Soil Dust Effects on Morphological, Physiological and Biochemical Responses of Four Tree Species of Semiarid Regions. *Eur. J. For. Res.* **2020**, *139*, 333–348. [CrossRef]
82. Siqueira-Silva, A.I.; Pereira, E.G.; Modolo, L.V.; Paiva, E.A.S. Leaf Structural Traits of Tropical Woody Species Resistant to Cement Dust. *Environ. Sci. Pollut. Res.* **2016**, *23*, 16104–16114. [CrossRef]
83. Nanos, G.D.; Ilias, I.F. Effects of Inert Dust on Olive (*Olea europaea* L.) Leaf Physiological Parameters. *Environ. Sci. Pollut. Res.-Int.* **2007**, *14*, 212–214. [CrossRef]
84. Farmer, A.M. The Effects of Dust on Vegetation—A Review. *Environ. Pollut.* **1993**, *79*, 63–75. [CrossRef]
85. Klein, T.; Yakir, D.; Buchmann, N.; Grünzweig, J.e.M. Towards an Advanced Assessment of the Hydrological Vulnerability of Forests to Climate Change-Induced Drought. *New Phytol.* **2014**, *201*, 712–716. [CrossRef]
86. Sperry, J.S.; Tyree, M.T. Mechanism of Water Stress-Induced Xylem Embolism. *Plant Physiol.* **1988**, *88*, 581–587. [CrossRef]
87. Andronis, V.; Karathanassi, V.; Tsalapati, V.; Kolokoussis, P.; Miltiadou, M.; Danezis, C. Time Series Analysis of Landsat Data for Investigating the Relationship between Land Surface Temperature and Forest Changes in Paphos Forest, Cyprus. *Remote Sens.* **2022**, *14*, 1010. [CrossRef]
88. Meyer, D. Classical Seasonal Decomposition by Moving Averages. *Recuper. El* **2018**, *30*.
89. Sax, C.; Eddelbuettel, D. Seasonal Adjustment by X-13arima-Seats in R. *J. Stat. Softw.* **2018**, *87*, 1–17. [CrossRef]
90. Cleveland, R.B.; Cleveland, W.S.; McRae, J.E.; Terpenning, I. STL: A Seasonal-Trend Decomposition. *J. Off. Stat* **1990**, *6*, 3–73.

91. Sun, Y.; Zhang, F. Quarterly Electricity Consumption Prediction Based on Time Series Decomposition Method and Gray Model. *Environ. Sci. Pollut. Res.* **2023**, *30*, 95410–95424. [CrossRef]
92. Verbesselt, J.; Hyndman, R.; Newnham, G.; Culvenor, D. Detecting Trend and Seasonal Changes in Satellite Image Time Series. *Remote Sens. Environ.* **2010**, *114*, 106–115. [CrossRef]
93. Dutrieux, L.P.; Verbesselt, J.; Kooistra, L.; Herold, M. Monitoring Forest Cover Loss Using Multiple Data Streams, a Case Study of a Tropical Dry Forest in Bolivia. *ISPRS J. Photogramm. Remote Sens.* **2015**, *107*, 112–125. [CrossRef]
94. Gao, Y.; Solórzano, J.V.; Quevedo, A.; Loya-Carrillo, J.O. How BFAST Trend and Seasonal Model Components Affect Disturbance Detection in Tropical Dry Forest and Temperate Forest. *Remote Sens.* **2021**, *13*, 2033. [CrossRef]
95. Hamunyela, E.; Rosca, S.; Mirt, A.; Engle, E.; Herold, M.; Gieseke, F.; Verbesselt, J. Implementation of BFASTmonitor Algorithm on Google Earth Engine to Support Large-Area and Sub-Annual Change Monitoring Using Earth Observation Data. *Remote Sens.* **2020**, *12*, 2953. [CrossRef]
96. Costa, H.; Giraldo, A.; Caetano, M. Exploring BFAST to Detect Forest Changes in Portugal. In Proceedings of the Image and Signal Processing for Remote Sensing XXVI; SPIE: Bellingham, WA, USA, 2020; Volume 11533, pp. 38–45.
97. Tecuapetla-Gómez, I.; Villamil-Cortez, G.; Cruz-López, M.I. On the Potential of BFAST for Monitoring Burned Areas Using Multi-Temporal Landsat-7 Images. *arXiv* **2019**, arXiv:1912.01543.
98. Gitas, I.Z.; Katagis, T.; Toukiloglou, P. Burned Area Mapping and Post-Fire Monitoring of a Mediterranean Forest Using NDVI Time-Series of Low Resolution Imagery and the BFAST Method Mapeamento de Área Queimada e Monitoramento Pós-Fogo de Floresta Na Região Mediterrânea a Partir de Série. *Ambiência* **2012**, *8*, 461–470. [CrossRef]
99. Xu, Y.; Yu, L.; Li, W.; Ciais, P.; Cheng, Y.; Gong, P. Annual Oil Palm Plantation Maps in Malaysia and Indonesia from 2001 to 2016. *Earth Syst. Sci. Data* **2020**, *12*, 847–867. [CrossRef]
100. Platt, R.V.; Manthos, D.; Amos, J. Estimating the Creation and Removal Date of Fracking Ponds Using Trend Analysis of Landsat Imagery. *Environ. Manag.* **2018**, *61*, 310–320. [CrossRef]
101. Che, X.; Yang, Y.; Feng, M.; Xiao, T.; Huang, S.; Xiang, Y.; Chen, Z. Mapping Extent Dynamics of Small Lakes Using Downscaling MODIS Surface Reflectance. *Remote Sens.* **2017**, *9*, 82. [CrossRef]
102. Yang, Y.; Wang, Y. Using the BFAST Algorithm and Multitemporal AIRS Data to Investigate Variation of Atmospheric Methane Concentration over Zoige Wetland of China. *Remote Sens.* **2020**, *12*, 3199. [CrossRef]
103. Zhang, Q.; Feng, T.; Wang, M.; Yang, G.; Lu, H.; Sun, W. A Twenty-Year Assessment of Spatiotemporal Variation of Surface Temperature in the Yangtze River Delta, China. *Remote Sens.* **2023**, *15*, 2274. [CrossRef]
104. Guo, B.; Hu, D.; Wang, Z.; Lin, A. Evolution of Gradual and Abrupt Trends in Nighttime Lights and Responses to Land Drivers via BFAST01 and Geographically Weighted Regression. *IEEE J. Sel. Top. Appl. Earth Obs. Remote Sens.* **2023**, *16*, 8609–8620. [CrossRef]
105. Delipetrou, P.; Makhzoumi, J.; Dimopoulos, P.; Georghiou, K. Cyprus. In *Mediterranean Island Landscapes*; Vogiatzakis, I., Pungetti, G., Mannion, A.M., Eds.; Springer: Dordrecht, The Netherlands, 2008.
106. Thirgood, J.V.; Myers, J.P.H. Cyprus: A Chronicle of Its Forests, Land and People. *Geogr. J.* **1989**, *155*, 117. [CrossRef]
107. Meikle, R.D. *Flora of Cyprus*; Bentham Moxon Trust, Royal Botanic Gardens: Richmond, UK, 1977.
108. Holmboe, J. *Studies on the Vegetation of Cyprus. Based upon Researches During the Spring and Summer 1905*; Bergens Museums: Bergen, Norway, 1914; Volume 10.
109. Bovill, A.K. *A Report on Plantation Work in Cyprus from 1879 to 1914*; US Government Printing Office: Washington, DC, USA, 1915.
110. Prodromou, M.; Theocharidis, C.; Gitas, I.Z.; Eliades, F.; Themistocleous, K.; Papasavvas, K.; Dimitrakopoulos, C.; Danezis, C.; Hadjimitsis, D. Forest Habitat Mapping in Natura2000 Regions in Cyprus Using Sentinel-1, Sentinel-2 and Topographical Features. *Remote Sens.* **2024**, *16*, 1373. [CrossRef]
111. Justice, C.O.; Townshend, J.R.G.; Vermote, E.F.; Masuoka, E.; Wolfe, R.E.; Saleous, N.; Roy, D.P.; Morisette, J.T. An Overview of MODIS Land Data Processing and Product Status. *Remote Sens. Environ.* **2002**, *83*, 3–15. [CrossRef]
112. Le Morvan, A.; Zribi, M.; Baghdadi, N.; Chanzy, A. Soil Moisture Profile Effect on Radar Signal Measurement. *Sensors* **2008**, *8*, 256–270. [CrossRef] [PubMed]
113. Akbari, V.; Solberg, S.; Puliti, S. Multitemporal Sentinel-1 and Sentinel-2 Images for Characterization and Discrimination of Young Forest Stands Under Regeneration in Norway. *IEEE J. Sel. Top. Appl. Earth Obs. Remote Sens.* **2021**, *14*, 5049–5063. [CrossRef]
114. Rouse, J.W., Jr.; Haas, R.H.; Deering, D.W.; Schell, J.A.; Harlan, J.C. *Monitoring the Vernal Advancement and Retrogradation (Green Wave Effect) of Natural Vegetation*; NASA: Washington, DC, USA, 1974.
115. Chuvieco, E.; Martin, M.P.; Palacios, A. Assessment of Different Spectral Indices in the Red-near-Infrared Spectral Domain for Burned Land Discrimination. *Int. J. Remote Sens.* **2002**, *23*, 5103–5110. [CrossRef]
116. Qiu, S.; Zhu, Z.; He, B. Fmask 4.0: Improved Cloud and Cloud Shadow Detection in Landsats 4–8 and Sentinel-2 Imagery. *Remote Sens. Environ.* **2019**, *231*, 111205. [CrossRef]

117. Neter, J.; Kutner, M.H.; Nachtsheim, C.J.; Wasserman, W. Applied Linear Statistical Models. 1996. Available online: https://d1b10bmlvqabco.cloudfront.net/attach/is282rqc4001vv/is6ccr3fl0e37q/iwfnjvgvl53z/Michael_H_Kutner_Christopher_J._Nachtsheim_JohnBookFi.org.pdf (accessed on 26 February 2025).
118. Verbesselt, J.; Zeileis, A.; Herold, M. Near Real-Time Disturbance Detection Using Satellite Image Time Series. *Remote Sens. Environ.* **2012**, *123*, 98–108. [CrossRef]
119. Verbesselt, J.; Hyndman, R.; Zeileis, A.; Culvenor, D. Phenological Change Detection While Accounting for Abrupt and Gradual Trends in Satellite Image Time Series. *Remote Sens. Environ.* **2010**, *114*, 2970–2980. [CrossRef]
120. Masiliūnas, D.; Tsendbazar, N.-E.; Herold, M.; Verbesselt, J. BFAST Lite: A Lightweight Break Detection Method for Time Series Analysis. *Remote Sens.* **2021**, *13*, 3308. [CrossRef]
121. Schultz, M.; Verbesselt, J.; Avitabile, V.; Souza, C.; Herold, M. Error Sources in Deforestation Detection Using BFAST Monitor on Landsat Time Series Across Three Tropical Sites. *IEEE J. Sel. Top. Appl. Earth Obs. Remote Sens.* **2016**, *9*, 3667–3679. [CrossRef]
122. Schultz, M.; Shapiro, A.; Clevers, J.G.P.W.; Beech, C.; Herold, M. Forest Cover and Vegetation Degradation Detection in the Kavango Zambezi Transfrontier Conservation Area Using BFAST Monitor. *Remote Sens.* **2018**, *10*, 1850. [CrossRef]
123. DeVries, B.; Verbesselt, J.; Kooistra, L.; Herold, M. Robust Monitoring of Small-Scale Forest Disturbances in a Tropical Montane Forest Using Landsat Time Series. *Remote Sens. Environ.* **2015**, *161*, 107–121. [CrossRef]
124. Kaufman, Y.J.; Tanre, D. Atmospherically Resistant Vegetation Index (ARVI) for EOS-MODIS. *IEEE Trans. Geosci. Remote Sens.* **1992**, *30*, 261–270. [CrossRef]
125. Rikimaru, A.; Roy, P.S.; Miyatake, S. Tropical Forest Cover Density Mapping. *Trop. Ecol.* **2002**, *43*, 39–47.
126. Huete, A.; Didan, K.; Miura, T.; Rodriguez, E.P.; Gao, X.; Ferreira, L.G. Overview of the Radiometric and Biophysical Performance of the MODIS Vegetation Indices. *Remote Sens. Environ.* **2002**, *83*, 195–213. [CrossRef]
127. Kumar, V.; Sharma, A.; Bhardwaj, R.; Thukral, A.K. Comparison of Different Reflectance Indices for Vegetation Analysis Using Landsat-TM Data. *Remote Sens. Appl. Soc. Environ.* **2018**, *12*, 70–77. [CrossRef]
128. Welikhe, P.; Quansah, J.E.; Fall, S. Elhenney WMc Estimation of Soil Moisture Percentage Using LANDSAT-Based Moisture Stress Index. *J. Remote Sens. GIS* **2017**, *6*, 2. [CrossRef]
129. Hais, M.; Jonášová, M.; Langhammer, J.; Kučera, T. Comparison of Two Types of Forest Disturbance Using Multitemporal Landsat TM/ETM+ Imagery and Field Vegetation Data. *Remote Sens. Environ.* **2009**, *113*, 835–845. [CrossRef]
130. Huang, S.; Tang, L.; Hupy, J.P.; Wang, Y.; Shao, G. A Commentary Review on the Use of Normalized Difference Vegetation Index (NDVI) in the Era of Popular Remote Sensing. *J. For. Res.* **2021**, *32*, 1–6. [CrossRef]
131. Gao, B.-C. NDWI—A Normalized Difference Water Index for Remote Sensing of Vegetation Liquid Water from Space. *Remote Sens. Environ.* **1996**, *58*, 257–266. [CrossRef]
132. Huete, A.R. A Soil-Adjusted Vegetation Index (SAVI). *Remote Sens. Environ.* **1988**, *25*, 295–309. [CrossRef]
133. Penuelas, J.; Filella, I.; Elvira, S.; Inclan, R. Reflectance Assessment of Summer Ozone Fumigated Mediterranean White Pine Seedlings. *Environ. Exp. Bot.* **1995**, *35*, 299–307. [CrossRef]
134. Zachariadis, T. Climate Change in Cyprus: Impacts and Adaptation Policies. *Cyprus Econ. Policy Rev.* **2012**, *6*, 21–37.
135. Molnár, T.; Király, G. Forest Disturbance Monitoring Using Cloud-Based Sentinel-2 Satellite Imagery and Machine Learning. *J. Imaging* **2024**, *10*, 14. [CrossRef]
136. Zhang, N.; Su, X.; Zhang, X.; Yao, X.; Cheng, T.; Zhu, Y.; Cao, W.; Tian, Y. Monitoring Daily Variation of Leaf Layer Photosynthesis in Rice Using UAV-Based Multi-Spectral Imagery and a Light Response Curve Model. *Agric. For. Meteorol.* **2020**, *291*, 108098. [CrossRef]
137. Mamouri, R.-E.; Ansmann, A.; Nisantzi, A.; Solomos, S.; Kallos, G.; Hadjimitsis, D.G. Extreme Dust Storm over the Eastern Mediterranean in September 2015: Satellite, Lidar, and Surface Observations in the Cyprus Region. *Atmos. Chem. Phys.* **2016**, *16*, 13711–13724. [CrossRef]
138. Kaskaoutis, D.G.; Dumka, U.C.; Rashki, A.; Psiloglou, B.E.; Gavriil, A.; Mofidi, A.; Petrinoli, K.; Karagiannis, D.; Kambezidis, H.D. Analysis of Intense Dust Storms over the Eastern Mediterranean in March 2018: Impact on Radiative Forcing and Athens Air Quality. *Atmos. Environ.* **2019**, *209*, 23–39. [CrossRef]
139. Monteiro, A.; Basart, S.; Kazadzis, S.; Votsis, A.; Gkikas, A.; Vandenbussche, S.; Tobias, A.; Gama, C.; García-Pando, C.P.; Terradellas, E.; et al. Multi-Sectoral Impact Assessment of an Extreme African Dust Episode in the Eastern Mediterranean in March 2018. *Sci. Total Environ.* **2022**, *843*, 156861. [CrossRef]